Cerebral oxygen metabolism from MRI susceptibility

Emma Biondetti [a,b,1], Junghun Cho [c,1], Hyunyeol Lee [d,e,*]

[a] Department of Neuroscience, Imaging and Clinical Sciences, "D'Annunzio University" of Chieti-Pescara, Chieti, Italy
[b] Institute for Advanced Biomedical Technologies, "D'Annunzio University" of Chieti-Pescara, Chieti, Italy
[c] Department of Biomedical Engineering, University at Buffalo, The State University of New York, New York, USA
[d] School of Electronic and Electrical Engineering, Kyungpook National University, Daegu, Republic of Korea
[e] Department of Radiology, University of Pennsylvania, Philadelphia, Pennsylvania, USA

ARTICLE INFO

ABSTRACT

This article provides an overview of MRI methods exploiting magnetic susceptibility properties of blood to assess cerebral oxygen metabolism, including the tissue oxygen extraction fraction (OEF) and the cerebral metabolic rate of oxygen ($CMRO_2$). The first section is devoted to describing blood magnetic susceptibility and its effect on the MRI signal. Blood circulating in the vasculature can have diamagnetic (oxyhemoglobin) or paramagnetic properties (deoxyhemoglobin). The overall balance between oxygenated and deoxygenated hemoglobin determines the induced magnetic field which, in turn, modulates the transverse relaxation decay of the MRI signal via additional phase accumulation. The following sections of this review then illustrate the principles underpinning susceptibility-based techniques for quantifying OEF and $CMRO_2$. Here, it is detailed whether these techniques provide global (OxFlow) or local (Quantitative Susceptibility Mapping - QSM, calibrated BOLD - cBOLD, quantitative BOLD - qBOLD, QSM+qBOLD) measurements of OEF or $CMRO_2$, and what signal components (magnitude or phase) and tissue pools they consider (intravascular or extravascular). Validations studies and potential limitations of each method are also described. The latter include (but are not limited to) challenges in the experimental setup, the accuracy of signal modeling, and assumptions on the measured signal. The last section outlines the clinical uses of these techniques in healthy aging and neurodegenerative diseases and contextualizes these reports relative to results from gold-standard PET.

1. Introduction

To support its metabolic function, the brain relies on a continuous oxygen supply via the arterial vasculature. Tissue utilization of oxygen can be estimated in the form of a physiological parameter called the oxygen extraction fraction (OEF). Substantial alterations to oxygen supply are thought to underlie several neurodegenerative diseases. This observation could make OEF a useful MRI-based marker of tissue health.

Various MRI-based methods enable the measurement of OEF by exploiting how oxygen and iron combine in the hemoglobin molecule, a mechanism rendering oxygenated blood diamagnetic and deoxygenated blood paramagnetic. Previous review articles have been written to sum-marize existing methods, their underlying mechanisms and potential clinical applications (Chen et al., 2022; Germuska and Wise, 2019; Jiang and Lu, 2022; Wehrli et al., 2017; Yablonskiy et al., 2013a) although we note that previous reviews have only focused on some of the methods presented here (Chen et al., 2022; Germuska and Wise, 2019; Wehrli et al., 2017; Yablonskiy et al., 2013a) or have provided fewer technical details, especially on combined methods, than we aim to do here (Jiang and Lu, 2022).

The present review has the following objectives: (1) To provide an overview of the magnetic susceptibility properties of blood and their contribution to the MRI signal. (2) To describe the principles of existing susceptibility-driven MRI oximetry methods. (3) To summarize recent

advances in such methods for quantifying cerebral oxygen metabolism, and to describe their use alone or in combination. (4) To summarize application studies using susceptibility-based MRI oximetry on human brain aging and neurodegenerative diseases.

In line with the scope of this Special Issue of the Journal, this article focuses on susceptibility-driven oximetry methods.

2. Background

2.1. Blood oxygenation, magnetic susceptibility, and MR signal

Magnetic susceptibility (χ) plays a critical role in determining MRI contrast because its spatial variations or temporal changes perturb the main magnetic field (B_0) and resultantly modulate both the magnitude and phase of the MR signal. In biological tissues, iron, due to its paramagnetic properties, is one of the major sources yielding the susceptibility-induced signal modulation. As such, MRI-based non-invasive quantification of iron deposition has been actively investigated in many neurological applications, for example, in the study of normal brain aging and neurodegenerative diseases. Recent articles (Ghassaban et al., 2019; Ropele and Langkammer, 2017) summarized techniques and studies relevant to iron quantification, and further discussed its separation into heme and non-heme iron (Yablonskiy et al., 2021).

Hemoglobin in red blood cells (RBC) is an essential substance as it carries oxygen from the lungs to organs enabling aerobic metabolism for energy production. Iron residing in hemoglobin is referred to as heme iron in distinction from nonheme iron found in the extravascular space (i.e., tissue). Importantly, hemoglobin's magnetism depends on its oxygenation states (Pauling and Coryell, 1936). The oxygen molecule, when bound to the Fe^{2+} ion in hemoglobin, yields no unpaired electrons and a zero total magnetic moment, thus making oxygenated hemoglobin (oHb) diamagnetic. Upon the release of oxygen, however, deoxygenated hemoglobin (dHb) exhibits paramagnetic properties because Fe^{2+} has four unpaired electrons. Thus, the magnetic susceptibility of blood (χ_{blood}) changes with its partial oxygen saturation (Y). χ_{blood} can be expressed by a volume-weighted sum of susceptibilities of four major components of blood (i.e., diamagnetic water, diamagnetic and paramagnetic components of Hb, and diamagnetic plasma) as (Cerdonio et al., 1981):

$$\chi_{blood} = \left\{ \left(1 - v_{Hb}\right) \cdot \chi_{water} + v_{Hb} \cdot \left[\chi_{protein} + (1 - Y) \cdot \chi_{dHb}\right] \right\} \cdot \text{Hct} + \chi_{plasma} \cdot (1 - \text{Hct}) \tag{1}$$

where v_{Hb} is the volume fraction of Hb in RBC, Hct is the hematocrit, and symbols with χ are self-explanatory in units of volume susceptibility. Hereafter, all units are in SI in which the scaling factor 4π is multiplied by susceptibility values in CGS units. With known values for v_{Hb} and susceptibilities, Spees et al. derived χ_{blood} as (Spees et al., 2001):

$$\chi_{blood} = 4\pi \cdot \{[0.264 \cdot (1 - Y) - 0.736]\text{Hct} - 0.722 \cdot (1 - \text{Hct})\} \text{ in ppm} \tag{2}$$

Of note, MRI is concerned with the relative susceptibility of blood ($\Delta\chi_{blood}$) in reference to the susceptibility of water. Given that the susceptibility difference between plasma ($\sim -4\pi \cdot 0.722$ ppm). and water ($\sim -4\pi \cdot 0.719$ ppm) is negligible (Weisskoff and Kiihne, 1992), $\Delta\chi_{blood}$ can be simplified to:

$$\Delta\chi_{blood} = \left[\Delta\chi_{do}(1 - Y) + \Delta\chi_{o}\right]\text{Hct} \tag{3}$$

Here, $\Delta\chi_{do}$ is the susceptibility difference between fully deoxygenated and fully oxygenated RBCs, and $\Delta\chi_{o}$ is the susceptibility difference between fully oxygenated RBC and water. Comparing Eqs. (2) and (3), $\Delta\chi_{do} = 4\pi \cdot 0.264$ ppm and $\Delta\chi_{o} = -4\pi \cdot 0.014$ ppm. These values were validated with two independent experiments (NMR and superconducting quantum interference device magnetometry) in (Spees et al., 2001), and more recently, were confirmed via image-based measurements of $\Delta\chi_{blood}$ in blood samples over a range of Y values (Jain et al., 2012).

History and relevant publications in regards to the relationship between $\Delta\chi_{blood}$ and Y have been summarized in great detail in a recent review article (Wehrli et al., 2017).

MR signal modulation in a voxel due to the susceptibility-induced magnetic field (ΔB_0) can be represented by:

$$S(t) = S_0 \cdot \exp\left(-R_2 t\right) \cdot \left\langle \exp\left(-i\gamma \Delta B_0(r)t\right) \right\rangle \tag{4}$$

where S_0 is the baseline signal at a time $t = 0$, R_2 is the radiofrequency (RF)-irreversible transverse relaxation rate manifested by an inhomogeneous magnetic field on a microscopic scale, γ is the gyromagnetic ratio ($\sim 2\pi \times 42.576 \times 10^6$ Hz/T), r is the spatial position within a voxel, and $\langle \cdot \rangle$ is the voxel-averaging operator. It is noted that Eq. (4) is valid for pulse sequences acquiring free-induction-decay or gradient-recalled echo (GRE) signals (i.e., those without collecting spin echoes) in a static dephasing regime (Yablonskiy and Haacke, 1994). Furthermore, under certain circumstances (discussed later), the $\langle \cdot \rangle$ operation in Eq. (4) can be rewritten as: $\exp(-R_2't) \cdot \exp(-i\gamma\langle\Delta B_0\rangle t)$ where R_2' is the RF-reversible transverse relaxation rate, closely related to $\Delta\chi_{blood}$ (Boxerman et al., 1995; Yablonskiy and Haacke, 1994). In such cases, the magnitude of S(t) is often represented by the effective transverse relaxation rate ($R_2^* = R_2 + R_2'$). Principles in phase- and magnitude-based quantification methods are discussed in the following sections. It is noted that blood R_2 ($=1/T_2$) also varies with blood's oxygenation level as a result of the intercellular chemical exchange and water diffusion in inhomogeneous fields on a microscopic scale (Li and van Zijl, 2020; Thulborn et al., 1982; Yablonskiy et al., 2013a). However, oximetry methods based on intravascular T_2 mapping (e.g., Bolar et al., 2011; Guo and Wong, 2012; Lu and Ge, 2008) are outside the scope of this Special Issue, and thus are deliberately omitted in this review.

2.2. Parameters measurable from MRI susceptibility

Metabolism is the process that produces energy mainly in the form of adenosine triphosphate (ATP) required for living cells to sustain their function. As almost the entirety of ATP production in the body is fulfilled by aerobic metabolism, knowledge of the oxygen consumption rate in organs, which is typically represented as the metabolic rate of oxygen (MRO_2) in units of µmol O_2 (or ml O_2) per minute per 100 g tissue, is important in evaluating their function. While relevant studies have been performed in nonbrain organs, for example, to assess breast tumors (Stadlbauer et al., 2019), placental function (Abaci Turk et al., 2019), peripheral vascular health (Englund and Langham, 2020), and renal oxygenation (Deshpande et al., 2022; Pedersen et al., 2005), a majority of oximetric techniques have so far been focused on the brain, aiming to quantify cerebral MRO_2 ($CMRO_2$). The scope of this review is thus restricted to the assessment of cerebral oxygen metabolism from MRI susceptibility.

Unfortunately, direct measurement of $CMRO_2$ presents a challenge as cerebral metabolism is tightly coupled with oxygen supply from arterial blood and oxygen extraction in the capillary bed. Instead, $CMRO_2$ is typically derived indirectly by resorting to the mass conservation law (as known as Fick's principle) expressed as:

$$CMRO_2 = C_a \cdot CBF \cdot \left(Y_a - Y_v\right) = C_a \cdot CBF \cdot Y_a \cdot OEF \tag{5}$$

Here, C_a is the oxygen carrying capacity of arterial blood in µmol O_2 per 100 ml blood, and is determined by $C_a = C_{hb} \cdot [\text{Hb}]$ where C_{hb} is the hemoglobin's oxygen carrying capacity (approximately 60 µmol O_2 per gram hemoglobin (Dominguez de Villota et al., 1981)). [Hb] is the hemoglobin concentration in units of gram hemoglobin per dL blood, ranging 14 – 18 g/dL and 12 – 16 g/dL in normal males and normal females, respectively (Walker and Hall, 1990). Considering the [Hb] variations across population, it is desirable to measure the value individually via blood draws or a finger stick test for $CMRO_2$ estimation accuracy. CBF is the cerebral blood flow in units of ml blood per minute per 100 g tissue, Y_a and Y_v are the hemoglobin oxygen saturation levels of arterial and venous blood, respectively, and $OEF = 1 - Y_v/Y_a$. Because arte-

rial blood is almost fully oxygenated, its contribution to susceptibility-related MR signal modulations in Eq. (4) is negligible, making it difficult to quantify Y_a from MR images. Instead, Y_a can be measured by a pulse oximeter or simply assumed ~100%. The two remaining parameters, CBF and Y_v, for $CMRO_2$ derivation are both MRI-measurable, but under completely different principles. As stated earlier, as Y_v quantification (or OEF) is directly related to MRI susceptibility, the following sections mainly focus on quantifying Y_v. In Sections 2.3 and 2.4, a brief overview of phase- and magnitude-based quantifications is provided, while in Section 3 pertinent methods are again classified into global- and local-scale measurements and technical details and validation studies in each class of methods are discussed.

2.3. Principle of phase-based quantification

In this class of methods, it is essential to obtain ΔB_0 maps using, for example, a spoiled gradient-recalled-echo (GRE) pulse sequence. Here, two or more echoes are successively acquired within each time of repetition (TR), and corresponding images at each echo time (TE) are then processed based on Eq. (4), yielding ΔB_0. Since the resulting ΔB_0 also contains a large-scale, background magnetic field ($\Delta B_{0,macro}$), accurate estimation of such contributions and their removal is the next crucial step before quantifying blood oxygenation.

It is well known that ΔB_0 in Eq. (4) is described as a spatial convolution of χ with the dipole kernel. A method streamlining step-by-step procedures involved in finding χ from ΔB_0 is generally referred to as quantitative susceptibility mapping (QSM) (de Rochefort et al., 2010). The method's technical advances and application studies are summarized in recent review articles (Deistung et al., 2017; Haacke et al., 2015; Vinayagamani et al., 2021; Wang and Liu, 2015; Wang et al., 2017). Given ΔB_0 with $\Delta B_{0,macro}$ eliminated, the spatial deconvolution problem can be solved to obtain voxel-wise susceptibility maps by various algorithms (QSM Challenge 2.0 Organization Committee et al., 2021; Kee et al., 2017), e.g., by computing $F(\Delta B_0)/(\frac{1}{3} - \frac{k_z^2}{k^2})$ directly in the frequency domain (i.e., k-space) (Salomir et al., 2003) where $F(\cdot)$ is the Fourier transform operator and k is the k-space position, and by using Bayesian approaches with physiological constraints (Liu et al., 2012). Hence, the QSM method is able to measure $\Delta\chi_{blood}$ in large draining veins (diameter >> voxel size), allowing for quantification of their oxygenation levels via Eq. (3), as was demonstrated in (Fan et al., 2014; Haacke et al., 2010; Xu et al., 2014). See Section 3.2.1.1 for more studies and a detailed discussion pertaining to this line of research.

Under certain circumstances, $\Delta\chi_{blood}$ of blood vessels can be calculated without such a dipole inversion (Fan et al., 2012; Fernández-Seara et al., 2006; Haacke et al., 1997; Jain et al., 2010). The method here, generally referred to as susceptometry-based oximetry (SBO), thus greatly simplifies the quantification procedure in the QSM-based technique above. Specifically, regarding a blood vessel as a long cylinder while correcting for the Lorentzian magnetic field contribution, the relationship between ΔB_0 inside the vessel ($\Delta B_{0,iv}$) and $\Delta\chi_{blood}$ can be expressed by the following linear equation:

$$\Delta B_{0,iv} = \frac{1}{2} B_0 \left(\cos^2\theta - \frac{1}{3} \right) \Delta\chi_{blood} \tag{6}$$

where θ is the angle of the vessel relative to the direction of B_0. Eq. (6) indicates that $\Delta\chi_{blood}$ (and thus Y) can be derived with both $\Delta B_{0,iv}$ and θ known. It is noted that while $\Delta B_{0,iv}$ is uniform within the vessel, dHb-induced magnetic field in the extravascular region is inhomogeneous but is averaged to zero over a circle encompassing the vessel (Schenck, 1996). Thus, $\Delta B_{0,iv}$ in reference to the surrounding tissue is readily obtained by calculating $\Delta\phi_{ie}/\gamma\Delta TE$ ($\Delta\phi_{ie}$: intra-to-extravascular phase difference and ΔTE: inter-echo spacing) in an inter-echo phase difference map. The angle θ can be measured in vessel scout images separately acquired, using, e.g., phase-contrast (PC) MRI. A second-order polynomial fitting was suggested as a simple means to eliminate the effect of $\Delta B_{0,macro}$ on the Y quantification (Langham et al., 2009b), while

various vessel geometries were examined theoretically and experimentally, concluding that the quantification using Eq. (6) is valid for vessels with $\theta < 30°$ (Langham et al., 2009a; Li et al., 2012). Techniques and studies based on this principle are discussed in Section 3.1.

For an imaging voxel comprising a tissue and surrounding blood vessels with varying orientations, induced magnetic fields cancel each other out across intra- and extra-vascular spaces, thus greatly reducing the phase sensitivity to $\Delta\chi_{blood}$. In this regard, the phase-based methods have been primarily targeting large vessels, although some work based on QSM with an isometabolic challenge (i.e., caffeine intake (Zhang et al., 2015) and hyperventilation (Zhang et al., 2017b)) has shown its feasibility in voxel-wise quantifications (see Section 3.2.1.2).

2.4. Principle of magnitude-based quantification

This class of methods employ particular models for signal modulations due to a blood vessel network (despite a number of assumptions being made (Yablonskiy et al., 2013a)) that link signal magnitudes directly to tissue oxygenation levels. Largely, the methods can be divided into two classes, namely, calibrated BOLD (cBOLD) (Blockley et al., 2013) and quantitative BOLD (qBOLD) (He and Yablonskiy, 2007). As the acronyms suggest, parameters that determine attainable BOLD contrast, i.e., dHb concentration ([dHb]) and deoxygenated blood volume (v), are either "calibrated" or "quantified". Given that a blood-to-tissue volume ratio in a voxel is very small (Hua et al., 2019), both methods often assume that the intravascular signal contribution is negligible and account for the extravascular compartment as a dominant signal source. Both techniques exploit the fact that magnetic field induced by dHb in the blood vessel network manifests as signal decays that can be described with R_2'. Hence, R_2' serves as an intermediary parameter with the following forms:

$$R_2' = A \cdot v \cdot [dHb]^\beta \tag{7}$$

in cBOLD (Hoge et al., 1999) where A is the scaling constant and β is an empirical constant that accounts for the effect of water diffusion in the presence of local magnetic field gradients, and

$$R_2' = \frac{1}{3} \cdot \gamma \cdot B_0 \cdot v \cdot \left(\Delta\chi_{blood} - \Delta\chi_n \right) \tag{8}$$

in qBOLD where $\Delta\chi_n$ is the susceptibility difference between non-blood neural tissue (χ_n) and water. It is noted that in the original qBOLD model (Yablonskiy and Haacke, 1994) the susceptibility difference between fully oxygenated blood and non-blood tissue was assumed to be negligible, and thereby Eq. (8) is simplified to:

$$R_2' = \frac{1}{3} \cdot \gamma \cdot B_0 \cdot v \cdot \Delta\chi_{do} \cdot Hct \cdot (1 - Y) \tag{9}$$

It is further noted that the above R_2' models are valid in the absence of other susceptibility sources such as non-heme iron and air. Nevertheless, in cBOLD dHb-related R_2' is calibrated with two sets of BOLD experiments from which the effect of non-dHb can be removed (see Section 3.2.2), while in recent qBOLD approaches such effect is included explicitly in quantification models (see Section 3.2.3).

While Eqs. (7) and (9) were determined empirically (Boxerman et al., 1995; Ogawa et al., 1993) and analytically (Yablonskiy and Haacke, 1994), the two R_2' models can be described in a unified framework. Here, the parameter β comes into play. When dHb-induced ΔB_0 changes rapidly relative to a diffusion length, water protons in the extravascular space experience additional dephasing, leading to increased R_2' (hence, $\beta > 1$). By contrast, when ΔB_0 is uniform over the diffusion path, the diffusion effect becomes insignificant, which is the case under the so-called 'static dephasing regime' (here, $\beta = 1$, and Eq. (9) can be reduced to Eq. (7) with $A \propto \frac{1}{3}\gamma B_0\Delta\chi_{do}$). β depends on a number of factors (Boxerman et al., 1995; Kiselev and Posse, 1999; Ogawa et al., 1993), including B_0, vessel size, and TE. The value of β has been found by measurements in a rat brain with a range of superparamagnetic iron oxide

concentrations (Shu et al., 2016), or from simulations using a mouse brain's microvascular model (Cheng et al., 2019). Once β is determined, R_2'-related, intermediate parameters are sought in both cBOLD and qBOLD (albeit with largely different approaches – see Sections 3.2.2 and 3.2.3) for quantification of oxygen metabolism.

3. Susceptibility-based quantification of cerebral oxygen metabolism

In this section, susceptibility-based brain oximetry techniques exploiting the above-mentioned contrast mechanisms are reviewed largely in two categories – global-scale and regional- or local-scale quantifications. Representative techniques in each class of methods are summarized in Table 1.

3.1. Global-scale measurement techniques

As discussed in Section 2.2, oxygen saturation of blood vessels conforming to certain geometries can be extracted from magnetic field maps using Eqs. (3) and (6). In this regard, the superior sagittal sinus (SSS) at the posterior level is a good candidate for measuring global OEF of the brain, as it is long and directs towards the direction of B_0 while draining about half of the total blood in the brain. Jain et al. (Jain et al., 2010) first applied this principle to global $CMRO_2$ estimation in a single pulse sequence, termed "OxFlow". Here, two 2D GRE modules differing in TE at a brain slice are applied alternately with 2D PC MRI (comprising flow-compensation and flow-encoding modules) at a neck level, yielding Y_v at SSS and total CBF, respectively, and finally global $CMRO_2$ via Eq. (5). With a temporal resolution of 30 s, the OxFlow technique allows dynamic $CMRO_2$ quantifications, as shown by Jain et al. (2011), which was also cross-validated with optical imaging in neonates with congenital heart disease (Jain et al., 2014).

Later, the original OxFlow pulse sequence was modified in several variants to speed up the data acquisition. Such attempts include three-interleaf OxFlow (dual-echo GRE and the two modules in PC MRI) (Barhoum et al., 2015a) and dual-band OxFlow (simultaneous excitation of brain and neck slices and image separation in a parallel MRI framework; Fig. 1) (Lee et al., 2017), achieving temporal resolution of 8 and 6 s, respectively. Additionally, a single-slice OxFlow method was introduced, in which the two PC modules are applied to the brain slice with both collecting dual-echo signals. Total CBF is then indirectly measured by scaling up the blood flow (BF) of SSS based on a calibration ratio between the two BF values obtained individually prior to actual dynamic $CMRO_2$ imaging. In combination with the view-sharing approach, the method achieves 2–3 s temporal resolution with both Cartesian (Rodgers et al., 2013) and radial (Cao et al., 2018) k-space sampling. The OxFlow method implemented in variable forms discussed above has so far found several applications, including patients with obstructed sleep apnea (Rodgers et al., 2016; Wu et al., 2022), healthy subjects during states of reduced consciousness such as sleep (Caporale et al., 2021), calibrating BOLD signal independently of isometabolicity of administered gas mixtures (Englund et al., 2020), and simultaneous PET/MRI-based rapid and noninvasive mapping of local $CMRO_2$ with OxFlow-derived global $CMRO_2$ serving as a reference to calibrate the $^{15}O-O_2$ tracer (Narciso et al., 2021).

The SBO technique has been compared with the T_2-based counterpart (termed "TRUST") for global OEF measurements (Lu and Ge, 2008). Barhoum et al. reported that SBO yielded a slightly lower baseline OEF than TRUST in 12 healthy subjects (Barhoum et al., 2015b). In (Rodgers et al., 2015), where both OxFlow and TRUST data were simultaneously obtained from a single pulse sequence, the authors also found in 10 healthy subjects at resting state that OEF in TRUST is higher than that in OxFlow. The same result was obtained in a separate study with nine healthy participants (Miao et al., 2019). The study also observed significant and nonsignificant OEF differences between the two methods under hypoxic and hypercapnic conditions, respectively, while showing in two healthy subjects that SBO-derived OEF values are in better agreement with co-oximeter measurement via internal jugular vein catheterization (Miao et al., 2019). Across all comparison studies above, the difference in baseline OEF measurements is no more than 8 percentage

Table 1
Summary of susceptibility-based MRI techniques for quantification of cerebral oxygen metabolism.

Technique	Measurement Scale	Analyzed Signal Components	Accounted Pools	Representative References	Notes
Susceptometry-Based Oximetry	Global	Phase	Intravascular	Fernández-Seara et al. (2006) Jain et al. (2010)	• Whole-brain average OEF • Readily combined with PC MRI for global $CMRO_2$ measurements • Dependence on vessel geometry
QSM-Based Oximetry	Local	Phase	Intravascular	Haacke et al. (2010) Fan et al. (2014)	• OEF for large veins • Dependence on QSM accuracy
			Intravascular / Extravascular	Zhang et al. (2015) Zhang et al. (2017b)	• Voxelwise OEF using four-pool susceptibility model • Need for separate CBF mapping • Isometabolic challenges required[*]
cBOLD	Local	Magnitude	Extravascular	Bulte et al. (2012) Gauthier and Hoge (2013) Wise et al. (2013)	• Voxelwise OEF via M (or R_2') calibration • ASL interleaved with BOLD acquisitions • Gas-breathing challenges required
qBOLD	Local	Magnitude	Extravascular	An and Lin (2000) He and Yablonskiy (2007)[**]	• Voxelwise OEF via R_2' mapping or by fitting Eq. (9) • Static dephasing regime assumed • Difficult to disentangle v and Y_v • Mostly 2D-limited
QSM+qBOLD	Local	Magnitude / Phase	Intravascular / Extravascular	Cho et al. (2018)	• Voxelwise OEF by combining QSM and qBOLD • 3D multi-echo GRE acquisitions • CBF mapping accompanied for v initialization[***]

[*] The need for isometabolic challenges is removed in (Zhang et al., 2018).

[**] Three pools (extravascular, intravascular, and interstitial/cerebrospinal fluid) are accounted for.

[***] The need for CBF mapping is obviated in (Cho et al., 2021c, 2020).
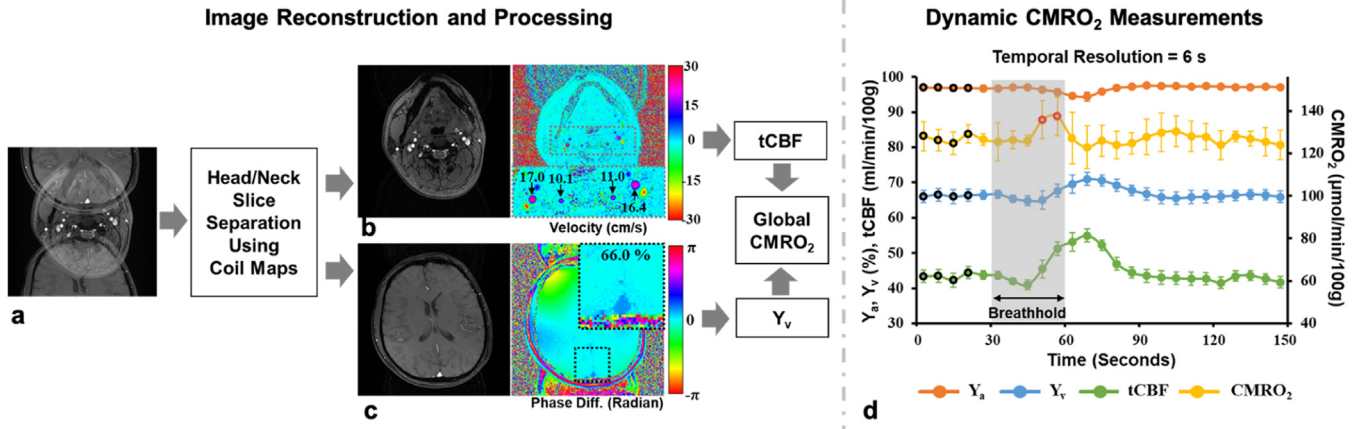
Fig. 1. Left: Image reconstruction and processing procedures in dual-band OxFlow. The slice-overlapped image (a) initially acquired is resolved using pre-determined coil sensitivity maps to yield separate neck (b) and brain (c) images, leading to tCBF and Y_v quantifications, respectively, and finally global $CMRO_2$. Right: Dual-band OxFlow-based quantification of time-varying Y_v, tCBF, and $CMRO_2$ in response to an apneic challenge. Group-averaged time-courses of the four physiologic quantities at baseline, breathhold (shaded area), and recovery periods (d). Reproduced from (Lee et al., 2017) with permission.

points. This discrepancy resulted likely from a systematic bias in each method, for example, due to imperfect removal of $\Delta B_{0,\text{macro}}$ in OxFlow and miscalibrated T_2-Y_v models in TRUST. Technical advances pertaining to TRUST and studies applying the method are extensively reviewed in recent article (Jiang and Lu, 2022). Additionally, a recent study has compared SBO with QSM for global OEF quantifications at 7 T, yielding a good correlation ($r = 0.88$) between the two methods (Lundberg et al., 2022).

3.2. Local-scale measurement techniques

3.2.1. QSM-based methods

QSM estimates voxel-wise susceptibility (χ). In the brain, χ can be divided into three contributions, 1) non-blood neural tissue susceptibility (χ_n), 2) plasma (χ_p) and 3) hemoglobin susceptibility that depends on the venous oxygenation, i.e., OEF effect (Zhang et al., 2015, 2017b):

$$\chi = (1 - CBV) \cdot \chi_n + CBV \cdot (1 - Hct) \cdot \chi_p + CBV \cdot Hct$$
$$\cdot \left[\Delta\chi_o + \Delta\chi_{\text{do}} \cdot \left\{ (1 - Y_v) \cdot \frac{v}{CBV} + (1 - Y_a) \cdot \left(\frac{CBV - v}{CBV} \right) \right\} \right] \quad (10)$$

where CBV, v is the total and venule cerebral blood volume fraction relative to voxel volume, respectively (dimensionless), Y_a and Y_v are the arterial and venous oxygenation, $Y_v = \frac{[Hb]-[dHb]_v}{[Hb]}$ and $Y_a = \frac{[Hb]-[dHb]_a}{[Hb]}$, where $[dHb]_v$ and $[dHb]_a$ is the concentration (μmol/mL) of deoxyhemoglobin in venules and arterioles, respectively. Note that Eq. (10) is based on a micro-vasculature where arteriole and venule hematocrit is similar to capillary hemotocrit, and it can be also expressed with using oxy- and dexoy-hemoglobin susceptibilities as in the original QSM-based OEF mapping (Zhang et al., 2018, 2015, 2017b). The χ estimated by QSM can be used for both macrovascular and microvascular OEF measurements, as is discussed in the following subsections.

3.2.1.1. Macrovascular OEF measurements.
The QSM-based macrovascular OEF method (hereafter termed "Quantitative Oxygenation Venography (QOV)") (Fan et al., 2014; Haacke et al., 2010), considers sole blood contribution in large veins. By setting $\chi_n = 0$, $CBV = v = 1$ and $CBV_a = 0$ in χ (Eq. (10)), the venous susceptibility (χ_{vein}) becomes a linear function of Y.

$$\chi_{vein}(Y_v) = [\Delta\chi_{\text{do}}(1 - Y_v) + \Delta\chi_o] \cdot Hct + (1 - Hct) \cdot \chi_p \quad (11)$$

Equation (11) is identical to Eq. (3) with assuming negligible plasma susceptibility ($\chi_p = 0$). Using a clinically practical multi-echo GRE sequence, QOV enabled venous oxygenation (Y_v) estimation for

any tilt angles of the vessel, that cannot be achieved by the MR susceptometry-based method discussed in Section 3.1 above (Fan et al., 2014).

QOV ignores the χ_p term as the plasma contribution is assumed to be much smaller than the hemoglobin contribution (Fan et al., 2014; Weisskoff and Kiihne, 1992). However, the assumption of negligible plasma contribution may not be valid for high venous oxygenation, e.g., the plasma contribution approaches 12% of the hemoglobin contribution when $Y_v = 0.75$ based on Eq. (11).

Validation studies:

The OEF from QOV showed a good correlation with 1) the OEF by dual-gas cBOLD in healthy subjects (Fan et al., 2016), 2) SBO in the SSS of healthy subjects (Lundberg et al., 2022) and human fetuses (Yadav et al., 2019), and 3) the PET-OEF in stroke patients, showing an elevated OEF in the affected hemispheres of the patients (Kudo et al., 2016). Compared to normal breathing, QOV detected the expected OEF decrease during hypercapnia (Fig. 2), which demonstrates the QOV-OEF sensitivity to physiological changes (Fan et al., 2015a). In a rat stroke model, QOV showed an increased Y_v in hyperoxia compared to normoxia, and its change was correlated with the oxygenation saturation change measured by R_2^* (Hsieh et al., 2017). Another rat stroke study provided comparable Y_v values to those estimated by a pulse oximeter in the longitudinal monitoring after reperfusion (Hsieh et al., 2016).

Possible issues and approaches:

As venous oxygenation, Y_v, linearly depends on the venous susceptibility, χ_{vein} (Eq. (11)), it is critical to estimate accurate χ_{vein} values. Veins generally have high positive susceptibility values compared to the surrounding brain tissue, e.g., $0.05 \sim 0.5$ ppm (Berg et al., 2021), and vessels with small diameters, e.g., ~2 mm at pial veins (Fan et al., 2015b), and flow. Hence, they may suffer from susceptibility underestimation by partial volume effects (Karsa et al., 2019; Zhou et al., 2017) and susceptibility quantification errors induced by uncompensated flow effects (Xu et al., 2014), which may lead to errors in venous oxygenation estimation. Finally, care must be taken when choosing the QSM reconstruction algorithm, as different QSM reconstruction mechanisms result in different venous susceptibility and oxygenation measurements (Berg et al., 2021).

To address these issues and improve the accuracy of QOV, the following approaches have been proposed: 1) using a QSM pipeline specific for accurate vein reconstruction (Berg et al., 2021; Biondetti et al., 2022; McFadden et al., 2021), 2) compensating partial volume effects (Ward et al., 2017a), and 3) developing accurate vein segmentation
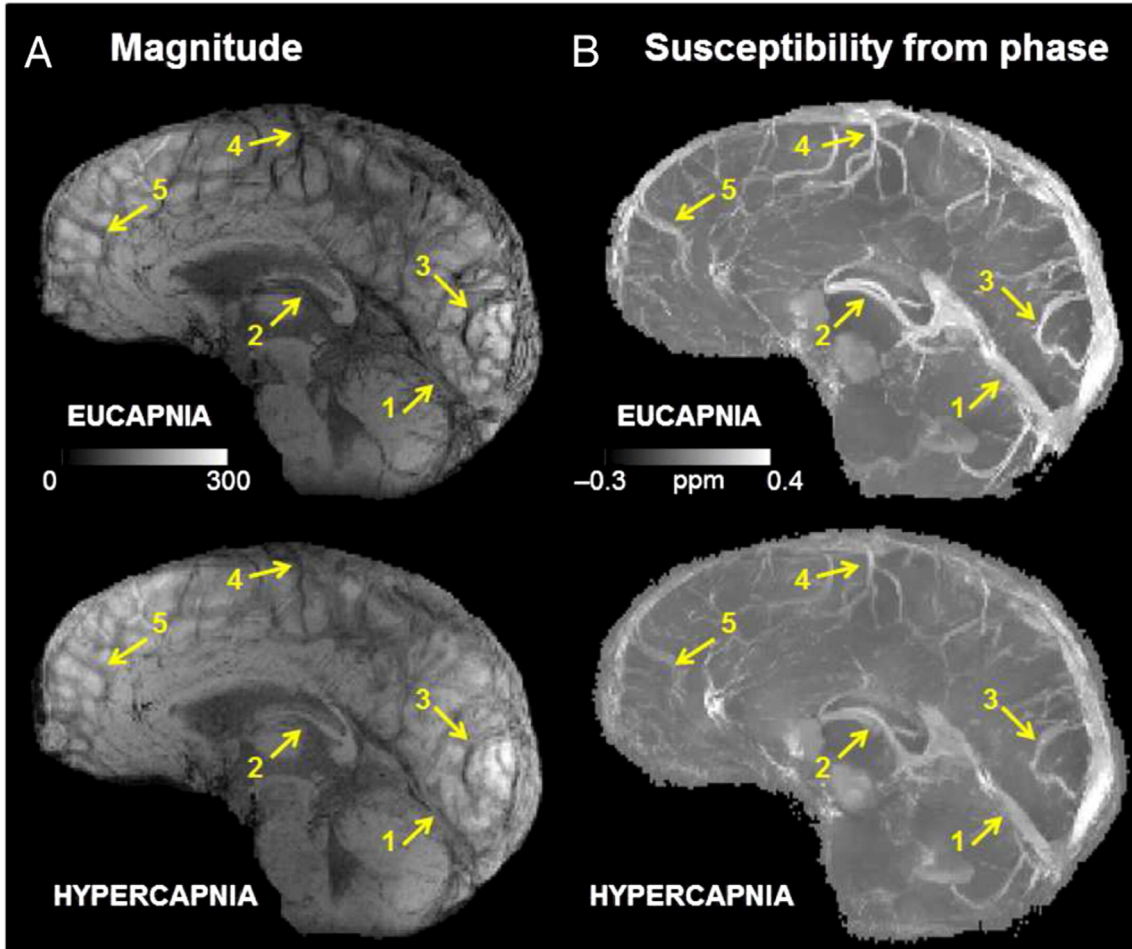
Fig. 2. (a) Minimum intensity projection of GRE magnitude images and (b) maximum intensity projections of quantitative susceptibility maps over 20-mm corresponding to eucapnia and hypercapnia in one subject. Note that the vessel contrast is diminished on both magnitude and susceptibility images due to decreased venous blood susceptibility during the hypercapnic state relative to the eucapnia. Yellow arrows indicate (1) the straight sinus, (2) the internal cerebral veins, (3) occipital pial veins, (4) parietal pial veins, and (5) frontal pial veins, in which relative OEF changes during hypercapnia were −42%, −40%, −55%, −56%, and −52%, respectively. Adapted from (Fan et al., 2015a) with permission.

algorithms (Bazin et al., 2016; Huck et al., 2019; Straub et al., 2022; Ward et al., 2018, 2017b).

3.2.1.2. Microvascular OEF measurements. The QSM-based microvascular OEF method (Zhang et al., 2015), i.e., QSM-OEF mapping, provides voxel-wise OEF maps with considering both blood and non-blood neural tissue contribution on χ (Fig. 3a). Eq. (10) can also be expressed in terms of 1) the ratio between v and CBV, $\alpha = 0.77$ (An and Lin, 2002b) and 2) $\chi_{ba} = Hct \cdot \Delta\chi_o + (1 - Hct) \cdot \chi_p$, the fully oxygenated blood susceptibility, ~ -0.1 ppm estimated by setting Hct = 0.357 (Zhang et al., 2015)

$$\chi(Y_v, v, \chi_n) = \left[\frac{\chi_{ba}}{\alpha} + Hct \cdot \Delta\chi_{do}\left(-Y_v + \frac{1 - (1 - \alpha) \cdot Y_a}{\alpha}\right) \right] \cdot v$$
$$+ \left(1 - \frac{v}{\alpha}\right) \cdot \chi_n \qquad (12)$$

where the two terms indicate the contribution of blood and non-blood tissue to the total susceptibility.

As χ is a function of three unknowns (Y_v, v, χ_n), OEF ($= 1 - Y_v/Y_a$) cannot be solved with one measurement of χ because the inversion is underdetermined. QSM-OEF mapping has devised several approaches to solve for Y_v. The first approach constructs two equations to solve for Y_v and χ_n (two unknowns) by using a vascular challenge, such as pre- vs.

post-caffeine (Zhang et al., 2015) or normal breathing vs. hyperventilation (Zhang et al., 2017b). The second approach applies a spatial and tissue-type constraint to solve Y_v and χ_n (two unknowns), i.e. by assuming the same constant $CMRO_2$ and χ_n within each tissue type (gray and white matter) across small regions of the brain (Zhang et al., 2018) to remove the clinically impractical vascular challenge (Fig. 3a). These approaches commonly treat v as a constant, estimated independently based on the linear relationship assumption between v and arterial spin labeling (ASL)-derived CBF (Zhang et al., 2018, 2015, 2017b).

Validation studies:

QSM-OEF mapping with hypercapnia showed a similar OEF with a small bias ($\sim$2%) compared to that from dual-gas cBOLD (Ma et al., 2020b) and agreed well with a hyperoxia-based QSM-OEF mapping in healthy subjects (Ma et al., 2020a).

Possible Issues and Approaches:

The commonly used linear relationship assumption between v and CBF was obtained by whole-brain linear regression in healthy adults (Leenders et al., 1990), so it may not be valid voxel-wise or in metabolic abnormalities in cerebrovascular disorders. To remove this unreliable assumption, QSM-OEF mapping was combined with qBOLD as the latter solves for v and the model combination (QSM+qBOLD=QQ) enables the utilization of both phase (QSM-OEF mapping) and magnitude (qBOLD) of multi-echo GRE signals (Cho et al., 2018).

(a) QSM   (b) qBOLD   (c) QQ (QSM+qBOLD)
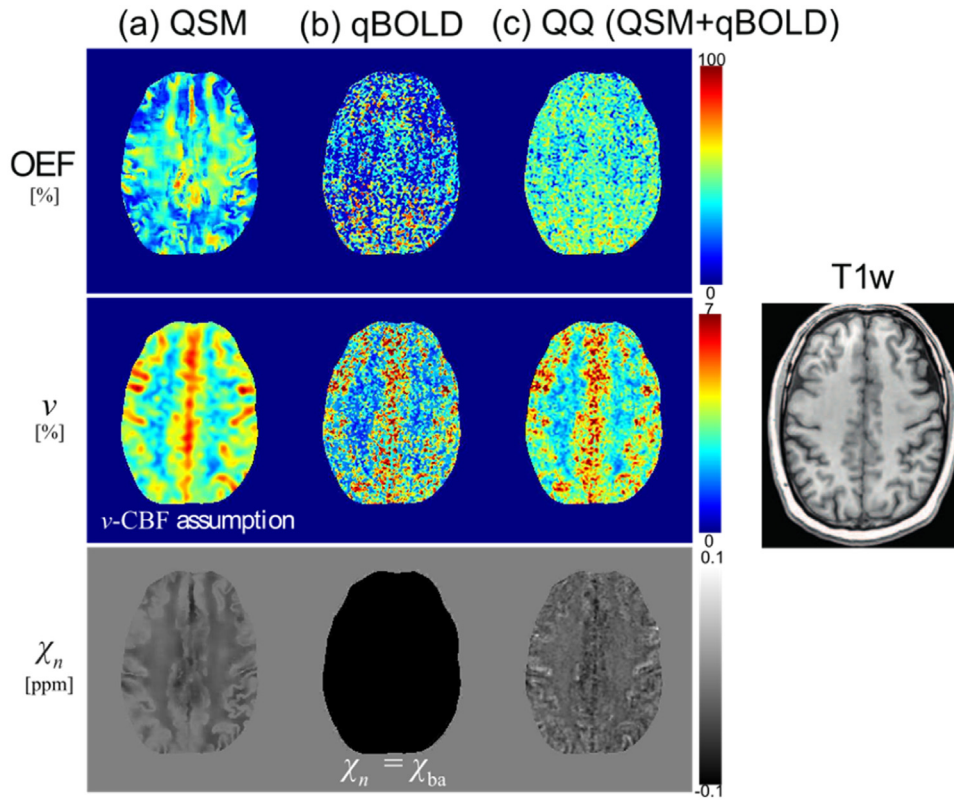
Fig. 3. Maps of oxygen extraction fraction (OEF), venous blood volume (v), non-blood neural tissue susceptibility (χ_n) in a healthy subject reconstructed using QSM-based microvascular method (QSM-OEF mapping), qBOLD, and QQ (QSM+qBOLD) from the same multi-echo gradient echo (GRE) dataset. Adapted from (Cho et al., 2018) with permission. (a) QSM-based microvascular OEF map was estimated by utilizing QSM maps calculated from GRE phase signals with assuming v to be known based on a linear relationship between v and CBF. (b) qBOLD-based OEF was obtained by utilizing the GRE magnitude signals with setting χ_n as constant (χ_{ba}) throughout an entire brain, $\chi_n = \chi_{ba}$. (c) QQ-based OEF is calculated by QQ, an integrated model of QSM and qBOLD which utilizes both GRE magnitude and phase signals without the assumptions in each qBOLD ($\chi_n = \chi_{ba}$) and QSM-OEF mapping ($v - CBF$ assumption).

3.2.2. Calibrated BOLD

In cBOLD, the intermediate parameter leading to measurements of oxygen metabolism is termed 'M', a calibration constant being related to R_2' by:

$$M = R_2' \cdot TE = A \cdot v \cdot [dHb]^\beta \cdot TE \tag{13}$$

To determine M, BOLD-weighted signals are acquired twice, one at a baseline state and one with an external stimulus (typically by means of gas breathing challenges), and compared. Specifically, by rearranging Eqs. (4) and (13), a relative change in the BOLD signal can be approximated as (Davis et al., 1998):

$$\frac{\Delta|S|}{|S_0|} \approx M \cdot \left(1 - \left(\frac{v}{v_0}\right)\left(\frac{[dHb]}{[dHb]_0}\right)^\beta\right) = M \cdot \left(1 - \left(\frac{CBF}{CBF_0}\right)^\alpha \left(\frac{[dHb]}{[dHb]_0}\right)^\beta\right) \tag{14}$$

Here, the subscript "0" refers to the baseline state, and $\Delta|S|$ is the magnitude signal difference between the two stages. Eq. (14) implies that M represents a maximum BOLD signal change if dHb would be completely replaced by oHb (i.e., [dHb]=0) due to the applied stimulus. The equality sign in Eq. (14) is based on Grubb's relationship (Grubb et al., 1974) with an empirical constant α. Since v measurements are yet challenging, it has been a convention that CBF is instead measured from ASL data (Alsop et al., 2015) acquired concurrently with the BOLD signal. Because $\alpha = 0.38$ in (Grubb et al., 1974) relates CBF to total CBV (rather than dHb-containing CBV), a BOLD-specific value of α was determined by later studies with neural stimulations ($\alpha \sim 0.23$) (Chen and Pike, 2009) and respiratory challenges ($\alpha \sim 0.18$) (Chen and Pike, 2010). As discussed in Section 2.4, the parameter β depends on several factors. $\beta \sim 1.3 - 1.5$ has been widely accepted at 3 T, and the value decreases with increasing B_0 (Gauthier and Fan, 2019).

The pioneering work (Davis et al., 1998) employed a (presumably) isometabolic hypercapnic stimulus to obviate the need for measuring [dHb], and a while later hyperoxia-based calibration (better tolerated than hypercapnia) was introduced in which [dHb] was obtained from partial pressure of end-tidal O_2 ($P_{ET}O_2$) measurements (Chiarelli et al., 2007). Once calibration has been achieved (i.e., M is known), the relative change in $CMRO_2$ in response to neural stimulation can be obtained, while approaches by means of dual-gas calibration enable baseline OEF and $CMRO_2$ mapping in absolute physiologic units (Bulte et al., 2012; Gauthier and Hoge, 2013). Furthermore, a generalized calibration protocol comprising multiple gas mixtures with different levels of hyperoxia and hypercapnia has been applied, and when compared with the dual-gas approach, allows for additional estimation of the parameters α and β (Wise et al., 2013) or improved stability in OEF and $CMRO_2$ mapping (Fan et al., 2016; Germuska et al., 2016). Despite being able to achieve high temporal resolution mapping of O_2 metabolism, cBOLD has been limited in clinical applications because of the need for specialized equipment and potential subject discomfort. A number of variants in this category and criticality of the assumptions (e.g., isometabolism of gas mixtures and uncertainty in α and β) have been reviewed in detail by recent articles (Bright et al., 2019; Chen et al., 2022; Germuska and Wise, 2019), and thus are not further discussed in this review.

3.2.3. Quantitative BOLD

qBOLD is a calibration-free technique, providing resting-state metabolic information without external stimuli or specialized equipment. The method distinguishes signal magnitude decay into three contributions: microscopic, dHb-induced mesoscopic, and macroscopic field inhomogeneities. The OEF estimation from qBOLD is related to the mesoscopic field inhomogeneity contribution, where the signal decay is driven by the susceptibility difference between blood vessel network and the surrounding tissue (Yablonskiy and Haacke, 1994).

In qBOLD, the following analytic form of the extravascular signal decay (F_{BOLD}) can be derived by assuming random orientations of blood vessels and a static dephasing regime (Yablonskiy and Haacke, 1994):

$$F_{BOLD}(Y_v, v, \chi_n, t) = exp[-v \cdot f_s(\delta\omega \cdot t)] \tag{15}$$

where f_s is the signal decay induced by the presence of the blood vessel network, which can be approximated to the following simple forms:

$f_S(\delta\omega \cdot t) \approx \frac{3}{10}(\delta\omega \cdot t)^2$ for $t \ll 1/\delta\omega$ and $f_S(\delta\omega \cdot t) \approx \delta\omega \cdot t$ for $t \gg 1/\delta\omega$ for short- and long-time scales, respectively (Yablonskiy and Haacke, 1994). $\delta\omega$ is the characteristic frequency due to the susceptibility difference between deoxygenated blood and the surrounding tissue (Cho et al., 2018): $\delta\omega(Y, \chi_n) = \frac{1}{3} \cdot \gamma \cdot B_0 \cdot [\text{Hct} \cdot \Delta\chi_{do} \cdot (1 - Y_v) + \chi_{ba} - \chi_n]$. Incorporating the effects of microscopic and macroscopic field inhomogeneities, the magnitude portion of Eq. (4) can be rewritten as (Ulrich and Yablonskiy, 2016):

$$S_{qBOLD}(S_0, R_2, Y_v, v, \chi_n, t) = S_0 \cdot e^{-R_2 \cdot t} \cdot F_{BOLD}(Y_v, v, \chi_n, t) \cdot G(t) \quad (16)$$

where $G(t)$ represents the $\Delta B_{0,\text{macro}}$-induced signal decay.

Based on the two distinctive signal decay patterns, qBOLD attempts to decouple v and Y_v. As discussed in Section 2.4, in the originally proposed qBOLD method (An and Lin, 2000; He and Yablonskiy, 2007) it was assumed that χ_n is a constant, which is set to be the fully oxygenated blood susceptibility value ($\chi_{ba} \sim -0.11$ *ppm*) (Zhang et al., 2015) throughout the whole brain, so that $\delta\omega$ can be treated as a function of Y as: $\delta\omega(Y_v) = \frac{1}{3} \cdot \gamma \cdot B_0 \cdot \text{Hct} \cdot \Delta\chi_{do} \cdot (1 - Y_v)$. Note further that R_2' in Eq. (9) can be obtained using the asymptotic behavior of Eq. (15) at long TEs. A comprehensive review on biophysical models pertinent to qBOLD can be found in (Yablonskiy et al., 2013a).

Regarding data acquisitions, there have been various pulse sequences employed for qBOLD parameter estimation. Earlier approaches such as gradient-echo sampling of spin-echo (GESSE) (He and Yablonskiy, 2007; Yablonskiy, 1998), gradient-echo sampling of free-induction-decay and echo (GESFIDE) (Christen et al., 2014; Ma and Wehrli, 1996), or asymmetric spin-echo (ASE) (Hoppel et al., 1993; Stone and Blockley, 2017) all rely on 180° RF pulse based spin-echo mechanisms, and thus are mostly limited to 2D quantifications due to relatively long scan times. Both GESSE and GESFIDE enable simultaneous R_2 and R_2' mapping, while ASE collects signals sensitive to R_2' only thus removing its dependency on R_2 in Eq. (16) (Ni et al., 2015). More recently, GRE-based methods have been introduced (Cho et al., 2018; Lee and Wehrli, 2021, 2022; Ulrich and Yablonskiy, 2016) for rapid 3D imaging across the entire brain, enabling both qBOLD and QSM analyses from a single data acquisition. Methods employing the spoiled GRE imaging separate R_2 and susceptibility-induced field inhomogeneity contributions during the qBOLD procedure (Cho et al., 2018; Ulrich and Yablonskiy, 2016), while those based on the non-spoiled GRE pulse sequence measure both R_2 and R_2' prior to qBOLD processing (Lee and Wehrli, 2021, 2022).

Validation studies:

In a tissue matrix phantom, qBOLD accurately estimated the volume fraction of the tissue matrix by separating the mesoscopic field inhomogeneity induced by the tissue matrix from macroscopic and microscopic field contributions (Yablonskiy, 1998). In rat brains, Y_v values measured using qBOLD showed a good agreement with oxygen saturation directly measured via a blood gas analyzer in the usage of two different anesthesia conditions (He et al., 2008) and under hypoxic, hypercapnic, and normoxic states (An et al., 2009).

Possible issues and approaches:

qBOLD is a multi-parameterized model, i.e., five unknowns (S_0, R_2, Y_v, v, χ_n) in the extravascular signal fitting (Eq. (16)), with the coupling between the parameters, particularly between v and Y_v. Hence, the method's attainable reproducibility is limited unless the SNR of acquired images is very high ($SNR \geq 500$), i.e., a small amount of noise can hinder the accurate estimation of v and Y_v (Lee et al., 2018; Sedlacik and Reichenbach, 2010; Wang et al., 2013). This may make the usage of qBOLD critically limited, in addition to specialized qBOLD imaging sequences that are difficult to implement.

There have been several approaches to improve the accuracy of qBOLD by 1) estimating the parameters separately using different sub-datasets in stepwise manners (An and Lin, 2000, 2002a, 2003; Cherukara et al., 2019; Stone and Blockley, 2017), 2) obtaining the coupled parameters individually using additional data acquisitions

(Christen et al., 2012; Domsch et al., 2014; Kaczmarz et al., 2019, 2020; Stone and Blockley, 2020), and 3) developing novel pulse sequences with imposing realistic constraints (Lee et al., 2018; Lee and Wehrli, 2022).

Furthermore, it is challenging in qBOLD to accurately distinguish Y_v (heme iron contribution) from other sources modulating the signal, such as $\Delta B_{0,\text{macro}}$ contribution (G in Eq. (16)) and non-blood tissue susceptibility (χ_n) contribution including non-heme iron. For instance, in the deep brain structures, the qBOLD may provide erroneous parameter estimates due to high non-heme iron content and strong macroscopic field effect near the sinus area. For an accurate G estimation, several approaches have been proposed, including voxel spread function (Ulrich and Yablonskiy, 2016; Yablonskiy et al., 2013b), z-shimming (Lee and Wehrli, 2022), and gradient-echo slice excitation profile imaging (Blockley and Stone, 2016). In parallel, recent qBOLD approaches have sought to address the effect of χ_n in combination with QSM. As mentioned above, the original qBOLD assumes χ_n as a constant equal to χ_{ba}, which may not be valid because the regional variation of χ_n, e.g., high positive χ_n in deep gray matter due to ferritin and negative χ_n in white matter due to myelin, is ignored. To remove this assumption, a recent approach combines qBOLD with QSM-based microvascular OEF (QSM+qBOLD=QQ) as the QSM method solves for χ_n (Cho et al., 2018).

3.2.4. Combined methods

An integrative model of QSM-OEF mapping and qBOLD, QQ (QSM+qBOLD=QQ), has been proposed to remove unnecessary and unrealistic assumptions in each model and to consider the OEF effect on both MRI magnitude and phase signal (Cho et al., 2018). QSM-OEF mapping utilizes the OEF effect on multi-echo GRE phase signal and assumes that v is known based on the linear relationship between v and CBF that is not realistic, whereas qBOLD can estimate v. On the other hand, qBOLD considers the OEF effect on multi-echo GRE magnitude signal and assume that χ_n is constant across the whole brain, whereas QSM-OEF mapping can estimate χ_n. Hence, by combining QSM-OEF mapping and qBOLD with both phase and magnitude components of multi-echo GRE signal utilized, QQ can estimate v and χ_n simultaneously. The more realistic and comprehensive signal modeling in QQ may lead to more reliable OEF (Fig. 3).

The QQ method has been validated in comparison to other modalities enabling OEF mapping. Compared with GESSE, a well-investigated sequence for qBOLD, QQ provided comparable OEF with using a routine multi-echo GRE sequence (Hubertus et al., 2019a). In healthy subjects, QQ provided OEF that agreed well with the OEF measured by dual-gas cBOLD (Cho et al., 2021a) with demonstrating its sensitivity to physiological OEF changes in response to hypercapnic gas breathing. Furthermore, QQ-based OEF is consistent with the reference standard ^{15}O-PET-based OEF (Cho et al., 2021b) in heathy adults with providing better scan-rescan reproducibility than ^{15}O-PET. In the meantime, the accuracy of QQ-OEF has been improved with machine learning that substantially improves SNR with clustering schemes (Cho et al., 2021c, 2020), artificial neural network (Hubertus et al., 2019b), and deep learning that is known to be effective in denoising (Cho et al., 2022) (Fig. 4).

QQ has demonstrated its feasibility in cerebrovascular disorders showing OEF abnormalities. In ischemic stroke (Wu et al., 2021; Zhang et al., 2020), QQ showed a significant OEF decrease in ischemic core from acute to subacute phase, whereas no change was found in other imaging biomarkers including $CMRO_2$, CBF, and ADC. This suggests that QQ-based OEF may be the most sensitive biomarker for tissue functional changes in stroke stages. In multiple sclerosis (Cho et al., 2022), QQ provided decreased OEF than healthy controls, which is consistent with progressive neurodegeneration, neural loss and atrophy in multiple sclerosis. QQ-based OEF further showed higher OEF in the QSM hyperintense rim within choric active MS lesions than the rest of the lesions, which agrees with active inflammation in the rim. In dementia
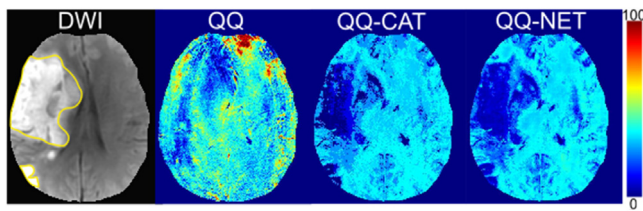
Fig. 4. QQ-based oxygen extraction fraction (OEF in percent) maps in an ischemic stroke patient (6 days post-onset) using different reconstruction algorithms, voxel-based gradient solver (QQ) (Cho et al., 2018), unsupervised machine learning (cluster analysis of time evolution, CAT) (Cho et al., 2020), and deep learning (NET) (Cho et al., 2022). QQ processed with machine learning (QQ-CAT) and deep learning (QQ-NET) captured low OEF values in a chronic ischemic stroke patient, which agrees with diffusion weighted imaging (DWI)-defined lesion (yellow contour in DWI). This suggests the improvement of QQ sensitivity to OEF abnormality.

(Chiang et al., 2022), QQ-based OEF showed positive associations with white matter hyperintensity, an important predictor of dementia. Also, QQ showed OEF abnormalities in brain tumor (Shen et al., 2021) and preeclampsia (Yang et al., 2022).

In parallel, a constrained qBOLD model (Lee and Wehrli, 2022) has been introduced in which R_2' derived from a steady-state-free-precession-based imaging method (Lee and Wehrli, 2021) is added as a constraint to the QQ model so as to separate heme and non-heme iron contributions to the measured R_2', while an additionally estimated venous blood volume map (Lee and Wehrli, 2020) is employed as a prior information for v, leading to 3D whole-brain qBOLD maps within physiologically plausible ranges (Fig. 5).

4. Applications to aging and neurodegeneration

Disentangling the effects of aging from those induced by pathology is essential to understand the mechanisms of neurodegenerative diseases typically associated with older age. In particular, measuring tissue OEF and $CMRO_2$ may be particularly relevant as mitochondrial dysfunction and altered oxygen metabolism have been associated with several neurodegenerative conditions (Bonda et al., 2011; Coskun et al., 2012; Reddy and Beal, 2005; Sullivan and Brown, 2005). To date, magnetic susceptibility-based MRI has been used to assess these physiological parameters in aging and dementia. The current section aims to review these studies. Because the gold standard for measuring $CMRO_2$ and OEF is PET, most commonly with ^{15}O-labeled radiotracers, this section also reports studies using PET for comparison with MRI. To provide a summary view of current applications, all studies discussed in this section are summarized in Table 2.

4.1. Aging

One study (Zhao et al., 2016) modeled OEF based on the BOLD contribution to the transverse relaxation rate ($R_2^* = 1/T_2^*$). Here, cortical OEF remained relatively constant across the adult lifespan, in line with earlier measurements of cortical OEF based on ^{15}O PET (Leenders et al., 1990; Pantano et al., 1984; Yamaguchi et al., 1986).

A different study using calibrated BOLD combined with periods of normocapnia, hypercapnia, and hyperoxia, found no difference between the whole-brain OEF of young and elderly healthy subjects but a higher regional OEF in the frontal and temporal cortex and the deep gray matter of younger subjects (De Vis et al., 2015). Moreover, in the younger compared to the elderly cohort, this study found a higher whole-brain $CMRO_2$ driven by a significantly higher $CMRO_2$ in the frontal, temporal, and parietal cortex and the deep gray matter (De Vis et al., 2015). These results were in line with PET studies finding a decrease in whole-brain $CMRO_2$ in elderly subjects (Leenders et al., 1990; Yamaguchi et al., 1986).

In one study (Ances et al., 2009) using BOLD fMRI with a hypercapnic calibration and stimulus-evoked BOLD fMRI, age did not affect the change in $CMRO_2$ in response to a visual stimulus. Another study (Hutchison et al., 2013) also using BOLD fMRI with a hypercapnic calibration and stimulus-evoked BOLD fMRI showed that the ratio between the change in cerebral blood flow and $CMRO_2$ in response to a visual stimulus decreases with age. These results, combined with further tests on behavioral status, suggested that cells affected by age-related cognitive decline require more oxygen to operate (Hutchison et al., 2013). Still, such an increased oxygen demand is not met by cerebral blood flow in older adults (Hutchison et al., 2013).

4.2. Cognitive impairment and dementia

One study (Chiang et al., 2022) combined QSM with qBOLD to assess OEF in clinical cohorts of cognitively impaired and healthy elderly subjects. Based on the hypothesis that cognitive impairment and dementia are predicted by age and white matter hyperintensities, this study investigated the effect of these two factors on OEF. In cognitively intact subjects, older age, but not white matter hyperintensity, was associated with lower OEF in the whole brain and the cortical gray matter. In contrast, in the cognitively impaired group, an increased burden of white matter hyperintensities, but not age, was significantly associated with lower OEF in the white matter. Moreover, cognitively impaired subjects had a higher regional OEF than cognitively intact subjects. The observed decrease in OEF with increasing age agreed with a study using ^{15}O PET (Eustache et al., 1995). However, this result was in contrast with studies using PET (Leenders et al., 1990; Marchal et al., 1992; Pantano et al., 1984; Yamaguchi et al., 1986), showing a decrease (Marchal et al., 1992; Peng et al., 2014) or no significant change in OEF with healthy aging (Leenders et al., 1990; Pantano et al., 1984; Yamaguchi et al., 1986). Thus, further work is needed to elucidate the global and regional relationship between OEF and age.

One study has used calibrated BOLD with periods of hypercapnia and hyperoxia to investigate oxygen metabolism in Alzheimer's disease patients relative to age-matched healthy controls (Lajoie et al., 2017). Here, patients had no significant decrease in age-corrected regional OEF and a significant decrease in $CMRO_2$ in the frontal, temporal, and parietal lobes (Lajoie et al., 2017). The observed decrease in regional $CMRO_2$ was consistent with earlier studies using ^{15}O PET (Frackowiak et al., 1981; Fukuyama et al., 1994; Ishii et al., 1996; Tohgi et al., 1998), whereas the absence of changes in OEF was in line with two of these studies (Frackowiak et al., 1981; Fukuyama et al., 1994) but in contrast with one study reporting a decreased OEF in the medial temporal lobe (Ishii et al., 1996) and another one reporting an increased OEF in the parietal lobe of patients (Tohgi et al., 1998).

One study on Alzheimer's disease (Liu et al., 2020) has used QSM to measure the average χ in various cerebral veins of patients relative to elderly healthy controls, based on the hypothesis that cerebral blood flow impairment in Alzheimer's disease may be associated with cognitive decline. The average venous χ was generally higher in patients than in controls, corresponding to lower venous oxygen levels. This result agrees with the higher OEF found by Chiang et al. in cognitively impaired subjects (Chiang et al., 2022). However, between-group differences in the average χ were only moderately significant in veins located in the thalamus and dentate nucleus (Liu et al., 2020). This study also found significant correlations between the average venous χ and clinical scores assessing cognitive status (i.e., the Mini-mental State Examination, Montréal Cognitive Assessment and Clock Drawing Task, and Activity of Daily Living Scale), demonstrating a relationship between the average venous χ and clinical cognitive assessment. Although these correlations involved variable sets of veins depending on the clinical score examined, they all appeared to involve a vein selected in the left dentate nucleus.
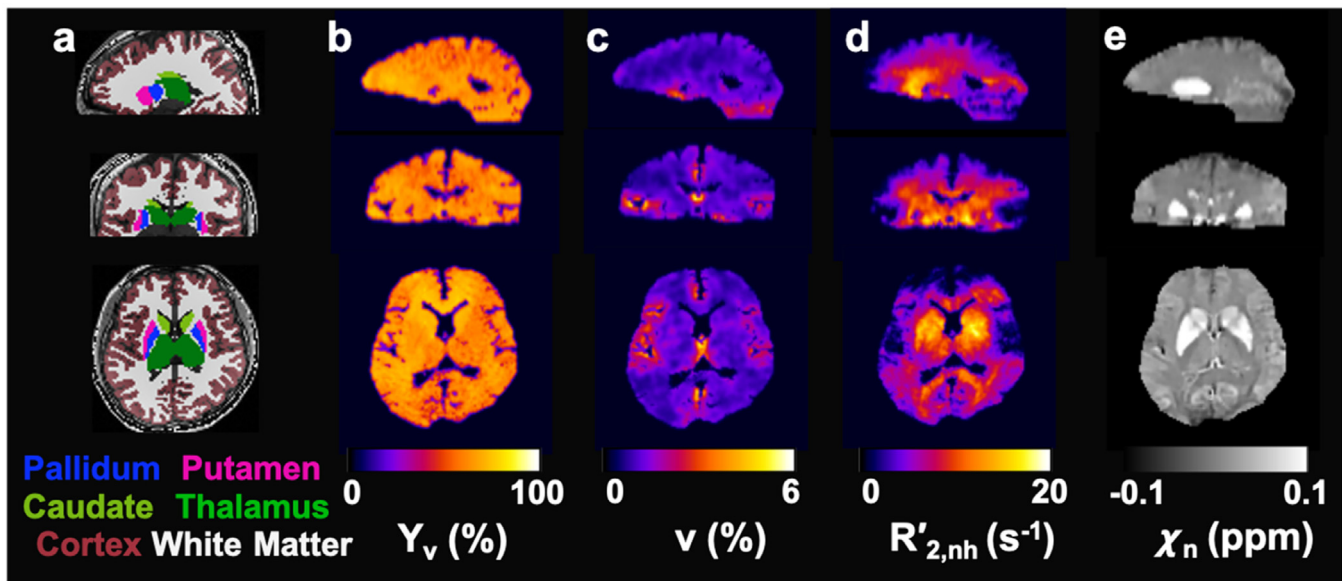
Fig. 5. Whole-brain 3D images in the three orthogonal planes in a representative study subject. a: color-coded six regions in the deep brain overlaid onto T_1-weighted MP-RAGE images. b-e: Quantitative maps of Y_v, v, $R'_{2,nh}$ (non-heme iron contribution to R'_2), and χ_n, obtained using the constrained qBOLD method (Lee and Wehrli, 2022). Note that all parameter maps depict expected contrast across brain territories, i.e., near-uniform distribution of Y_v (b), distinction between cortical gray and white matter in v (c), and highlighted deep brain structures in both $R'_{2,nh}$ (d) and χ_n (e).

Table 2
Clinical findings on oxygen metabolism from susceptibility-based MRI techniques.

Reference	Population	Technique	Number of subjects (M/F)	Subject age (mean ± SD; range) [years]	Findings
Chiang et al. (2022)	Healthy controls and cognitively impaired patients	QSM + qBOLD	Controls: 32 (9/23) Patients: 68 (27/41)	Controls: 69 ± 9.9; 50–87 Patients: 72 ± 8.4; 50–86	In the whole brain and the cortical gray matter of cognitively intact subjects, older age was associated with lower OEF; in the white matter of cognitively impaired subjects, more white matter hyperintensities were associated with lower OEF; cognitively impaired subjects had a higher regional OEF than cognitively intact subjects
Liu et al. (2020)	Healthy controls and patients with Alzheimer's disease	QSM-based oximetry	Controls: 22 (12/10) Patients: 59 (21/38)	Controls: 67.9 ± 8.6; n/a Patients: 71.1 ± 9.2; n/a	Patients had a higher OEF than controls
Zhao et al. (2016)	Healthy	qBOLD	20 (7/13)	44.2 ± 15.1; 22–74	OEF was constant with increasing age
De Vis et al. (2015)	Healthy, divided into young and elderly groups	Dual-gas cBOLD	Young: 16 (7/9) Elderly: 30 (17/13)	Young: 28 ± 3; 24–33 Elderly: 66 ± 4; 60–76	Whole-brain OEF was similar in the two groups; younger subjects had a higher OEF in the frontal, and temporal cortex, and the deep gray matter; younger subjects had a higher whole-brain $CMRO_2$ and a higher $CMRO_2$ in the frontal, temporal and parietal cortex and the deep gray matter
Hutchison et al. (2013)	Healthy, divided into young and elderly groups	cBOLD	Young: 11 (5/6) Elderly: 11 (5/6)	Young: 28.2 ± n/a; 23–33 Elderly: 60.5 ± n/a; 53–72	The ratio between changes in cerebral blood flow and $CMRO_2$ in response to a visual stimulus decreases with age
Ances et al., (2009)	Healthy, divided into young and elderly groups	cBOLD	Young: 10 (6/4) Elderly: 10 (6/4)	Young: 28 ± n/a; 21–35 Elderly: 53 ± n/a; 45–60	Age did not influence stimulus-evoked changes in $CMRO_2$

$CMRO_2$ = cerebral metabolic rate of oxygen; M/F = males/females; n/a = information was unavailable; OEF = oxygen extraction fraction; (q/c)BOLD = (quantitative/calibrated) blood oxygenation level dependent; QSM = quantitative susceptibility mapping; SD = standard deviation.

5. Conclusions

OEF and $CMRO_2$ are essential, direct biomarkers for cerebral tissue viability and function. This review covers MRI techniques that model susceptibility-induced modulation of magnitude and phase signal for quantification of OEF and $CMRO_2$ and their clinical applications to ag-ing and neurodegenerative diseases. Though respective MRI techniques have provided promising preliminary results, any of them has not been widely used clinically. It is partly because there has been no rigorous validation, e.g., accurately measuring physiological OEF abnormality in neurologic disorders, and also because any technique has not been publicly available via open-source codes for reproducibility test and broader

use. By resolving these issues, these MRI techniques may be valuable tools for cerebral oxygen metabolism quantification in neurodegenerative disorders.

Data and code availability statement

This is a review article in which no data and code are used.

Declaration of Competing Interest

None.

Credit authorship contribution statement

Emma Biondetti: Conceptualization, Formal analysis, Data curation, Investigation, Visualization, Writing – original draft, Writing – review & editing. **Junghun Cho:** Conceptualization, Formal analysis, Data curation, Investigation, Visualization, Writing – original draft, Writing – review & editing. **Hyunyeol Lee:** Conceptualization, Formal analysis, Data curation, Investigation, Visualization, Writing – original draft, Writing – review & editing, Supervision.

Data availability

No data was used for the research described in the article.

References

Abaci Turk, E., Stout, J.N., Ha, C., Luo, J., Gagoski, B., Yetisir, F., Golland, P., Wald, L.L., Adalsteinsson, E., Robinson, J.N., Roberts, D.J., Barth Jr., W.H., Grant, P.E., 2019. Placental MRI: developing accurate quantitative measures of oxygenation. Top Magn. Reson. Imaging 28, 285–297.

Alsop, D.C., Detre, J.A., Golay, X., Günther, M., Hendrikse, J., Hernandez-Garcia, L., Lu, H., MacIntosh, B.J., Parkes, L.M., Smits, M., 2015. Recommended implementation of arterial spin-labeled perfusion MRI for clinical applications: a consensus of the ISMRM perfusion study group and the European consortium for ASL in dementia. Magn. Reson. Med. 73, 102–116.

An, H., Lin, W., 2000. Quantitative measurements of cerebral blood oxygen saturation using magnetic resonance imaging. J. Cereb. Blood Flow Metab. 20, 1225–1236.

An, H., Lin, W., 2002a. Cerebral oxygen extraction fraction and cerebral venous blood volume measurements using MRI: effects of magnetic field variation. Magn. Reson. Med. 47, 958–966.

An, H., Lin, W., 2002b. Cerebral venous and arterial blood volumes can be estimated separately in humans using magnetic resonance imaging. Magn. Reson. Med. 48, 583–588.

An, H., Lin, W., 2003. Impact of intravascular signal on quantitative measures of cerebral oxygen extraction and blood volume under normo- and hypercapnic conditions using an asymmetric spin echo approach. Magn. Reson. Med. 50, 708–716.

An, H., Liu, Q., Chen, Y., Lin, W., 2009. Evaluation of MR-derived cerebral oxygen metabolic index in experimental hyperoxic hypercapnia, hypoxia, and ischemia. Stroke 40, 2165–2172.

Ances, B.M., Liang, C.L., Leontiev, O., Perthen, J.E., Fleisher, A.S., Lansing, A.E., Buxton, R.B., 2009. Effects of aging on cerebral blood flow, oxygen metabolism, and blood oxygenation level dependent responses to visual stimulation. Hum. Brain Mapp. 30, 1120–1132.

Barhoum, S., Langham, M.C., Magland, J.F., Rodgers, Z.B., Li, C., Rajapakse, C.S., Wehrli, F.W., 2015a. Method for rapid MRI quantification of global cerebral metabolic rate of oxygen. J. Cereb. Blood Flow Metab. 35, 1616–1622.

Barhoum, S., Rodgers, Z.B., Langham, M., Magland, J.F., Li, C., Wehrli, F.W., 2015b. Comparison of MRI methods for measuring whole-brain venous oxygen saturation. Magn. Reson. Med. 73, 2122–2128.

Bazin, P.L., Plessis, V., Fan, A.P., Villringer, A., Gauthier, C.J., 2016. Vessel segmentation from quantitative susceptibility maps for local oxygenation venography. In: 2016 IEEE 13th International Symposium on Biomedical Imaging (ISBI), pp. 1135–1138.

Berg, R.C., Preibisch, C., Thomas, D.L., Shmueli, K., Biondetti, E., 2021. Investigating the effect of flow compensation and quantitative susceptibility mapping method on the accuracy of venous susceptibility measurement. Neuroimage 240, 118399.

Biondetti, E., Karsa, A., Grussu, F., Battiston, M., Yiannakas, M.C., Thomas, D.L., Shmueli, K., 2022. Multi-echo quantitative susceptibility mapping: how to combine echoes for accuracy and precision at 3 Tesla. Magn. Reson. Med. 88, 2101–2116.

Blockley, N.P., Griffeth, V.E., Simon, A.B., Buxton, R.B., 2013. A review of calibrated blood oxygenation level-dependent (BOLD) methods for the measurement of task-induced changes in brain oxygen metabolism. NMR Biomed. 26, 987–1003.

Blockley, N.P., Stone, A.J., 2016. Improving the specificity of R2′ to the deoxyhaemoglobin content of brain tissue: prospective correction of macroscopic magnetic field gradients. Neuroimage 135, 253–260.

Bolar, D.S., Rosen, B.R., Sorensen, A.G., Adalsteinsson, E., 2011. QUantitative Imaging of eXtraction of oxygen and TIssue consumption (QUIXOTIC) using venular-targeted velocity-selective spin labeling. Magn. Reson. Med. 66, 1550–1562.

Bonda, D.J., Smith, M.A., Perry, G., Lee, H.G., Wang, X., Zhu, X., 2011. The mitochondrial dynamics of Alzheimer's disease and Parkinson's disease offer important opportunities for therapeutic intervention. Curr. Pharm. Des. 17, 3374–3380.

Boxerman, J.L., Hamberg, L.M., Rosen, B.R., Weisskoff, R.M., 1995. MR contrast due to intravascular magnetic susceptibility perturbations. Magn. Reson. Med. 34, 555–566.

Bright, M.G., Croal, P.L., Blockley, N.P., Bulte, D.P., 2019. Multiparametric measurement of cerebral physiology using calibrated fMRI. Neuroimage 187, 128–144.

Bulte, D.P., Kelly, M., Germuska, M., Xie, J., Chappell, M.A., Okell, T.W., Bright, M.G., Jezzard, P., 2012. Quantitative measurement of cerebral physiology using respiratory-calibrated MRI. Neuroimage 60, 582–591.

Cao, W., Chang, Y.V., Englund, E.K., Song, H.K., Barhoum, S., Rodgers, Z.B., Langham, M.C., Wehrli, F.W., 2018. High-speed whole-brain oximetry by golden-angle radial MRI. Magn. Reson. Med. 79, 217–223.

Caporale, A., Lee, H., Lei, H., Rao, H., Langham, M.C., Detre, J.A., Wu, P.H., Wehrli, F.W., 2021. Cerebral metabolic rate of oxygen during transition from wakefulness to sleep measured with high temporal resolution OxFlow MRI with concurrent EEG. J. Cereb. Blood Flow Metab. 41, 780–792.

Cerdonio, M., Morante, S., Vitale, S., 1981. Magnetic susceptibility of hemoglobins. Methods Enzymol. 76, 354–371.

Chen, J.J., Pike, G.B., 2009. BOLD-specific cerebral blood volume and blood flow changes during neuronal activation in humans. NMR Biomed. 22, 1054–1062.

Chen, J.J., Pike, G.B., 2010. MRI measurement of the BOLD-specific flow-volume relationship during neuronal activation. Neuroimage 53, 383–391.

Chen, J.J., Uthayakumar, B., Hyder, F., 2022. Mapping oxidative metabolism in the human brain with calibrated fMRI in health and disease. J. Cereb. Blood Flow Metab. 42, 1139–1162.

Cheng, X., Berman, A.J.L., Polimeni, J.R., Buxton, R.B., Gagnon, L., Devor, A., Sakadžić, S., Boas, D.A., 2019. Dependence of the MR signal on the magnetic susceptibility of blood studied with models based on real microvascular networks. Magn. Reson. Med. 81, 3865–3874.

Cherukara, M.T., Stone, A.J., Chappell, M.A., Blockley, N.P., 2019. Model-based Bayesian inference of brain oxygenation using quantitative BOLD. Neuroimage 202, 116106.

Chiang, G.C., Cho, J., Dyke, J., Zhang, H., Zhang, Q., Tokov, M., Nguyen, T., Kovanlikaya, I., Amoashiy, M., de Leon, M., Wang, Y., 2022. Brain oxygen extraction and neural tissue susceptibility are associated with cognitive impairment in older individuals. J. Neuroimaging 32, 697–709.

Chiarelli, P.A., Bulte, D.P., Wise, R., Gallichan, D., Jezzard, P., 2007. A calibration method for quantitative BOLD fMRI based on hyperoxia. Neuroimage 37, 808–820.

Cho, J., Kee, Y., Spincemaille, P., Nguyen, T.D., Zhang, J., Gupta, A., Zhang, S., Wang, Y., 2018. Cerebral metabolic rate of oxygen (CMRO2) mapping by combining quantitative susceptibility mapping (QSM) and quantitative blood oxygenation level-dependent imaging (qBOLD). Magn. Reson. Med. 80, 1595–1604.

Cho, J., Lee, J., An, H., Goyal, M.S., Su, Y., Wang, Y., 2021b. Cerebral oxygen extraction fraction (OEF): comparison of challenge-free gradient echo QSM+qBOLD (QQ) with 15O PET in healthy adults. J. Cereb. Blood Flow Metab. 41, 1658–1668 0271678X20973951.

Cho, J., Ma, Y., Spincemaille, P., Pike, G.B., Wang, Y., 2021a. Cerebral oxygen extraction fraction: comparison of dual-gas challenge calibrated BOLD with CBF and challenge-free gradient echo QSM+qBOLD. Magn. Reson. Med. 85, 953–961.

Cho, J., Nguyen, T.D., Huang, W., Sweeney, E.M., Luo, X., Kovanlikaya, I., Zhang, S., Gillen, K.M., Spincemaille, P., Gupta, A., Gauthier, S.A., Wang, Y., 2022. Brain oxygen extraction fraction mapping in patients with multiple sclerosis. J. Cereb. Blood Flow Metab. 42, 338–348. 271678X211048031.

Cho, J., Spincemaille, P., Nguyen, T.D., Gupta, A., Wang, Y., 2021c. Temporal clustering, tissue composition, and total variation for mapping oxygen extraction fraction using QSM and quantitative BOLD. Magn. Reson. Med. 86, 2635–2646.

Cho, J., Zhang, J., Spincemaille, P., Zhang, H., Hubertus, S., Wen, Y., Jafari, R., Zhang, S., Nguyen, T.D., Dimov, A.V., Gupta, A., Wang, Y., 2022. QQ-NET - using deep learning to solve quantitative susceptibility mapping and quantitative blood oxygen level dependent magnitude (QSM+qBOLD or QQ) based oxygen extraction fraction (OEF) mapping. Magn. Reson. Med. 87, 1583–1594.

Cho, J., Zhang, S., Kee, Y., Spincemaille, P., Nguyen, T.D., Hubertus, S., Gupta, A., Wang, Y., 2020. Cluster analysis of time evolution (CAT) for quantitative susceptibility mapping (QSM) and quantitative blood oxygen level-dependent magnitude (qBOLD)-based oxygen extraction fraction (OEF) and cerebral metabolic rate of oxygen (CMRO2) mapping. Magn. Reson. Med. 83, 844–857.

Christen, T., Pannetier, N.A., Ni, W.W., Qiu, D., Moseley, M.E., Schuff, N., Zaharchuk, G., 2014. MR vascular fingerprinting: a new approach to compute cerebral blood volume, mean vessel radius, and oxygenation maps in the human brain. Neuroimage 89, 262–270.

Christen, T., Schmiedeskamp, H., Straka, M., Bammer, R., Zaharchuk, G., 2012. Measuring brain oxygenation in humans using a multiparametric quantitative blood oxygenation level dependent MRI approach. Magn. Reson. Med. 68, 905–911.

Bilgic, B., Langkammer, C., Marques, J.P., Meineke, J., Milovic, C., Schweser, F.QSM Challenge 2.0 Organization Committee, 2021. QSM reconstruction challenge 2.0: design and report of results. Magn. Reson. Med. 86, 1241–1255.

Coskun, P., Wyrembak, J., Schriner, S.E., Chen, H.W., Marciniack, C., Laferla, F., Wallace, D.C., 2012. A mitochondrial etiology of Alzheimer and Parkinson disease. Biochim. Biophys. Acta 1820, 553–564.

Davis, T.L., Kwong, K.K., Weisskoff, R.M., Rosen, B.R., 1998. Calibrated functional MRI: mapping the dynamics of oxidative metabolism. Proc. Natl. Acad. Sci. 95, 1834–1839.

de Rochefort, L., Liu, T., Kressler, B., Liu, J., Spincemaille, P., Lebon, V., Wu, J., Wang, Y., 2010. Quantitative susceptibility map reconstruction from MR phase data using Bayesian regularization: validation and application to brain imaging. Magn. Reson. Med. 63, 194–206.

De Vis, J.B., Hendrikse, J., Bhogal, A., Adams, A., Kappelle, L.J., Petersen, E.T., 2015. Age-related changes in brain hemodynamics; a calibrated MRI study. Hum. Brain Mapp. 36, 3973–3987.

Deistung, A., Schweser, F., Reichenbach, J.R., 2017. Overview of quantitative susceptibility mapping. NMR Biomed. 30, e3569.

Deshpande, R.S., Langham, M.C., Wehrli, F.W., 2022. Quantification of bilateral whole-organ renal metabolic rate of O 2 by exploiting conservation of flow and mass principle: a preliminary study. In: Proceedings of Joint Annual Meeting ISMRM-ESMRMB, p. 4011.

Dominguez de Villota, E.D., Ruiz Carmona, M.T., Rubio, J.J., de Andrés, S., 1981. Equality of the in vivo and in vitro oxygen-binding capacity of haemoglobin in patients with severe respiratory disease. Br. J. Anaesth. 53, 1325–1328.

Domsch, S., Mie, M.B., Wenz, F., Schad, L.R., 2014. Non-invasive multiparametric qBOLD approach for robust mapping of the oxygen extraction fraction. Zeitschrift für Medizinische Physik 24, 231–242.

Englund, E.K., Fernández-Seara, M.A., Rodríguez-Soto, A.E., Lee, H., Rodgers, Z.B., Vidorreta, M., Detre, J.A., Wehrli, F.W., 2020. Calibrated fMRI for dynamic mapping of CMRO2 responses using MR-based measurements of whole-brain venous oxygen saturation. J. Cereb. Blood Flow Metab. 40, 1501–1516.

Englund, E.K., Langham, M.C., 2020. Quantitative and dynamic MRI measures of peripheral vascular function. Front. Physiol. 11, 120.

Eustache, F., Rioux, P., Desgranges, B., Marchal, G., Petit-Taboué, M.C., Dary, M., Lechevalier, B., Baron, J.C., 1995. Healthy aging, memory subsystems and regional cerebral oxygen consumption. Neuropsychologia 33, 867–887.

Fan, A.P., Benner, T., Bolar, D.S., Rosen, B.R., Adalsteinsson, E., 2012. Phase-based regional oxygen metabolism (PROM) using MRI. Magn. Reson. Med. 67, 669–678.

Fan, A.P., Bilgic, B., Gagnon, L., Witzel, T., Bhat, H., Rosen, B.R., Adalsteinsson, E., 2014. Quantitative oxygenation venography from MRI phase. Magn. Reson. Med. 72, 149–159.

Fan, A.P., Evans, K.C., Stout, J.N., Rosen, B.R., Adalsteinsson, E., 2015a. Regional quantification of cerebral venous oxygenation from MRI susceptibility during hypercapnia. Neuroimage 104, 146–155.

Fan, A.P., Govindarajan, S.T., Kinkel, R.P., Madigan, N.K., Nielsen, A.S., Benner, T., Tinelli, E., Rosen, B.R., Adalsteinsson, E., Mainero, C., 2015b. Quantitative Oxygen Extraction Fraction from 7-Tesla MRI Phase: reproducibility and Application in Multiple Sclerosis. J. Cereb. Blood Flow Metab. 35, 131–139.

Fan, A.P., Schäfer, A., Huber, L., Lampe, L., von Smuda, S., Möller, H.E., Villringer, A., Gauthier, C.J., 2016. Baseline oxygenation in the brain: correlation between respiratory-calibration and susceptibility methods. Neuroimage 125, 920–931.

Fernández-Seara, M.A., Techawiboonwong, A., Detre, J.A., Wehrli, F.W., 2006. MR susceptometry for measuring global brain oxygen extraction. Magn. Reson. Med. 55, 967–973.

Frackowiak, R.S.J., Pozzilli, C., Legg, N.J., Boulay, G.H., Marshall, J., Lenzi, G.L., Jones, T., 1981. Regional cerebral oxygen supply and utilization in dementia: a clinical and physiological study with oxygen-15 and positron emission tomography. Brain 104, 753–778.

Fukuyama, H., Ogawa, M., Yamauchi, H., Yamaguchi, S., Kimura, J., Yonekura, Y., Konishi, J., 1994. Altered cerebral energy metabolism in Alzheimer's disease: a PET study. J. Nucl. Med. 35, 1–6.

Gauthier, C.J., Fan, A.P., 2019. BOLD signal physiology: models and applications. Neuroimage 187, 116–127.

Gauthier, C.J., Hoge, R.D., 2013. A generalized procedure for calibrated MRI incorporating hyperoxia and hypercapnia. Hum. Brain Mapp. 34, 1053–1069.

Germuska, M., Merola, A., Murphy, K., Babic, A., Richmond, L., Khot, S., Hall, J.E., Wise, R.G., 2016. A forward modelling approach for the estimation of oxygen extraction fraction by calibrated fMRI. Neuroimage 139, 313–323.

Germuska, M., Wise, R.G., 2019. Calibrated fMRI for mapping absolute CMRO2: practicalities and prospects. Neuroimage 187, 145–153.

Ghassaban, K., Liu, S., Jiang, C., Haacke, E.M., 2019. Quantifying iron content in magnetic resonance imaging. Neuroimage 187, 77–92.

Grubb Jr., R.L., Raichle, M.E., Eichling, J.O., Ter-Pogossian, M.M., 1974. The effects of changes in PaCO2 on cerebral blood volume, blood flow, and vascular mean transit time. Stroke 5, 630–639.

Guo, J., Wong, E.C., 2012. Venous oxygenation mapping using velocity-selective excitation and arterial nulling. Magn. Reson. Med. 68, 1458–1471.

Haacke, E.M., Lai, S., Reichenbach, J.R., Kuppusamy, K., Hoogenraad, F.G.C., Takeichi, H., Lin, W., 1997. In vivo measurement of blood oxygen saturation using magnetic resonance imaging: a direct validation of the blood oxygen level-dependent concept in functional brain imaging. Hum. Brain Mapp. 5, 341–346.

Haacke, E.M., Liu, S., Buch, S., Zheng, W., Wu, D., Ye, Y., 2015. Quantitative susceptibility mapping: current status and future directions. Magn. Reson. Imaging 33, 1–25.

Haacke, E.M., Tang, J., Neelavalli, J., Cheng, Y.C., 2010. Susceptibility mapping as a means to visualize veins and quantify oxygen saturation. J. Magn. Reson. Imaging 32, 663–676.

He, X., Yablonskiy, D.A., 2007. Quantitative BOLD: mapping of human cerebral deoxygenated blood volume and oxygen extraction fraction: default state. Magn. Reson. Med. 57, 115–126.

He, X., Zhu, M., Yablonskiy, D.A., 2008. Validation of oxygen extraction fraction measurement by qBOLD technique. Magn. Reson. Med. 60, 882–888.

Hoge, R.D., Atkinson, J., Gill, B., Crelier, G.R., Marrett, S., Pike, G.B., 1999. Investigation of BOLD signal dependence on cerebral blood flow and oxygen consumption: the deoxyhemoglobin dilution model. Magn. Reson. Med. 42, 849–863.

Hoppel, B.E., Weisskoff, R.M., Thulborn, K.R., Moore, J.B., Kwong, K.K., Rosen, B.R., 1993. Measurement of regional blood oxygenation and cerebral hemodynamics. Magn. Reson. Med. 30, 715–723.

Hsieh, M.-C., Kuo, L.-W., Huang, Y.-A., Chen, J.-H., 2017. Investigating hyperoxic effects in the rat brain using quantitative susceptibility mapping based on MRI phase. Magn. Reson. Med. 77, 592–602.

Hsieh, M.-C., Tsai, C.-Y., Liao, M.-C., Yang, J.-L., Su, C.-H., Chen, J.-H., 2016. Quantitative susceptibility mapping-based microscopy of magnetic resonance venography (QSM-mMRV) for in vivo morphologically and functionally assessing cerebromicrovasculature in rat stroke model. PLoS ONE 11, e0149602.

Hua, J., Liu, P., Kim, T., Donahue, M., Rane, S., Chen, J.J., Qin, Q., Kim, S.G., 2019. MRI techniques to measure arterial and venous cerebral blood volume. Neuroimage 187, 17–31.

Hubertus, S., Thomas, S., Cho, J., Zhang, S., Wang, Y., Schad, L.R., 2019a. Comparison of gradient echo and gradient echo sampling of spin echo sequence for the quantification of the oxygen extraction fraction from a combined quantitative susceptibility mapping and quantitative BOLD (QSM+qBOLD) approach. Magn. Reson. Med. 82, 1491–1503.

Hubertus, S., Thomas, S., Cho, J., Zhang, S., Wang, Y., Schad, L.R., 2019b. Using an artificial neural network for fast mapping of the oxygen extraction fraction with combined QSM and quantitative BOLD. Magn. Reson. Med. 82, 2199–2211.

Huck, J., Wanner, Y., Fan, A.P., Jäger, A.T., Grahl, S., Schneider, U., Villringer, A., Steele, C.J., Tardif, C.L., Bazin, P.L., Gauthier, C.J., 2019. High resolution atlas of the venous brain vasculature from 7 T quantitative susceptibility maps. Brain Struct. Funct. 224, 2467–2485.

Hutchison, J.L., Lu, H., Rypma, B., 2013. Neural mechanisms of age-related slowing: the ΔCBF/ΔCMRO2 ratio mediates age-differences in BOLD signal and human performance. Cereb. Cortex 23, 2337–2346.

Ishii, K., Kitagaki, H., Kono, M., Mori, E., 1996. Decreased medial temporal oxygen metabolism in Alzheimer's disease shown by PET. J. Nucl. Med. 37, 1159–1165.

Jain, V., Abdulmalik, O., Propert, K.J., Wehrli, F.W., 2012. Investigating the magnetic susceptibility properties of fresh human blood for noninvasive oxygen saturation quantification. Magn. Reson. Med. 68, 863–867.

Jain, V., Buckley, E.M., Licht, D.J., Lynch, J.M., Schwab, P.J., Naim, M.Y., Lavin, N.A., Nicolson, S.C., Montenegro, L.M., Yodh, A.G., Wehrli, F.W., 2014. Cerebral oxygen metabolism in neonates with congenital heart disease quantified by MRI and optics. J. Cereb. Blood Flow Metab. 34, 380–388.

Jain, V., Langham, M.C., Floyd, T.F., Jain, G., Magland, J.F., Wehrli, F.W., 2011. Rapid magnetic resonance measurement of global cerebral metabolic rate of oxygen consumption in humans during rest and hypercapnia. J. Cereb. Blood Flow Metab. 31, 1504–1512.

Jain, V., Langham, M.C., Wehrli, F.W., 2010. MRI estimation of global brain oxygen consumption rate. J. Cereb. Blood Flow Metab. 30, 1598–1607.

Jiang, D., Lu, H., 2022. Cerebral oxygen extraction fraction MRI: techniques and applications. Magn. Reson. Med. 88, 575–600.

Kaczmarz, S., Göttler, J., Zimmer, C., Hyder, F., Preibisch, C., 2019. Characterizing white matter fiber orientation effects on multi-parametric quantitative BOLD assessment of oxygen extraction fraction. J. Cereb. Blood Flow Metab. 40, 760–774.

Kaczmarz, S., Hyder, F., Preibisch, C., 2020. Oxygen extraction fraction mapping with multi-parametric quantitative BOLD MRI: reduced transverse relaxation bias using 3D-GraSE imaging. Neuroimage 220, 117095.

Karsa, A., Punwani, S., Shmueli, K., 2019. The effect of low resolution and coverage on the accuracy of susceptibility mapping. Magn. Reson. Med. 81, 1833–1848.

Kee, Y., Liu, Z., Zhou, L., Dimov, A., Cho, J., Rochefort, L.d., Seo, J.K., Wang, Y., 2017. Quantitative susceptibility mapping (QSM) algorithms: mathematical rationale and computational implementations. IEEE Trans. Biomed. Eng. 64, 2531–2545.

Kiselev, V.G., Posse, S., 1999. Analytical model of susceptibility-induced MR signal dephasing: effect of diffusion in a microvascular network. Magn. Reson. Med. 41, 499–509.

Kudo, K., Liu, T., Murakami, T., Goodwin, J., Uwano, I., Yamashita, F., Higuchi, S., Wang, Y., Ogasawara, K., Ogawa, A., Sasaki, M., 2016. Oxygen extraction fraction measurement using quantitative susceptibility mapping: comparison with positron emission tomography. J. Cereb. Blood Flow Metab. 36, 1424–1433.

Lajoie, I., Nugent, S., Debacker, C., Dyson, K., Tancredi, F.B., Badhwar, A., Belleville, S., Deschaintre, Y., Bellec, P., Doyon, J., Bocti, C., Gauthier, S., Arnold, D., Kergoat, M.-J., Chertkow, H., Monchi, O., Hoge, R.D., 2017. Application of calibrated fMRI in Alzheimer's disease. NeuroImage Clin. 15, 348–358.

Langham, M.C., Magland, J.F., Epstein, C.L., Floyd, T.F., Wehrli, F.W., 2009a. Accuracy and precision of MR blood oximetry based on the long paramagnetic cylinder approximation of large vessels. Magn. Reson. Med. 62, 333–340.

Langham, M.C., Magland, J.F., Floyd, T.F., Wehrli, F.W., 2009b. Retrospective correction for induced magnetic field inhomogeneity in measurements of large-vessel hemoglobin oxygen saturation by MR susceptometry. Magn. Reson. Med. 61, 626–633.

Lee, H., Englund, E.K., Wehrli, F.W., 2018. Interleaved quantitative BOLD: combining extravascular R2' - and intravascular R2-measurements for estimation of deoxygenated blood volume and hemoglobin oxygen saturation. Neuroimage 174, 420–431.

Lee, H., Langham, M.C., Rodriguez-Soto, A.E., Wehrli, F.W., 2017. Multiplexed MRI methods for rapid estimation of global cerebral metabolic rate of oxygen consumption. Neuroimage 149, 393–403.

Lee, H., Wehrli, F.W., 2020. Venous cerebral blood volume mapping in the whole brain using venous-spin-labeled 3D turbo spin echo. Magn. Reson. Med. 84, 1991–2003.

Lee, H., Wehrli, F.W., 2021. Alternating unbalanced SSFP for 3D R2' mapping of the human brain. Magn. Reson. Med. 85, 2391–2402.

Lee, H., Wehrli, F.W., 2022. Whole-brain 3D mapping of oxygen metabolism using constrained quantitative BOLD. Neuroimage 250, 118952.

Leenders, K.L., Perani, D., Lammertsma, A.A., Heather, J.D., Buckingham, P., Healy, M.J., Gibbs, J.M., Wise, R.J., Hatazawa, J., Herold, S., et al., 1990. Cerebral blood flow, blood volume and oxygen utilization. Normal values and effect of age. Brain 113 (Pt 1), 27–47.

Li, C., Langham, M.C., Epstein, C.L., Magland, J.F., Wu, J., Gee, J., Wehrli, F.W., 2012. Accuracy of the cylinder approximation for susceptometric measurement of intravascular oxygen saturation. Magn. Reson. Med. 67, 808–813.

Li, W., van Zijl, P.C.M., 2020. Quantitative theory for the transverse relaxation time of blood water. NMR Biomed. 33, e4207.

Liu, J., Liu, T., de Rochefort, L., Ledoux, J., Khalidov, I., Chen, W., Tsiouris, A.J., Wisnieff, C., Spincemaille, P., Prince, M.R., Wang, Y., 2012. Morphology enabled dipole inversion for quantitative susceptibility mapping using structural consistency between the magnitude image and the susceptibility map. Neuroimage 59, 2560–2568.

Liu, Y., Dong, J., Song, Q., Zhang, N., Wang, W., Gao, B., Tian, S., Dong, C., Liang, Z., Xie, L., Miao, Y., 2020. Correlation between cerebral venous oxygen level and cognitive status in patients with Alzheimer's disease using quantitative susceptibility mapping. Front. Neurosci. 14, 570848.

Lu, H., Ge, Y., 2008. Quantitative evaluation of oxygenation in venous vessels using T2-Relaxation-Under-Spin-Tagging MRI. Magn. Reson. Med. 60, 357–363.

Lundberg, A., Lind, E., Olsson, H., Helms, G., Knutsson, L., Wirestam, R., 2022. Comparison of MRI methods for measuring whole-brain oxygen extraction fraction under different geometric conditions at 7T. J. Neuroimaging 32, 442–458.

Ma, J., Wehrli, F.W., 1996. Method for image-based measurement of the reversible and irreversible contribution to the transverse-relaxation rate. J. Magn. Reson. Ser. B 111, 61–69.

Ma, Y., Mazerolle, E.L., Cho, J., Sun, H., Wang, Y., Pike, G.B., 2020a. Quantification of brain oxygen extraction fraction using QSM and a hyperoxic challenge. Magn. Reson. Med. 84, 3271–3285.

Ma, Y., Sun, H., Cho, J., Mazerolle, E.L., Wang, Y., Pike, G.B., 2020b. Cerebral OEF quantification: a comparison study between quantitative susceptibility mapping and dual–gas calibrated BOLD imaging. Magn. Reson. Med. 83, 68–82.

Marchal, G., Rioux, P., Petit-Taboué, M.C., Sette, G., Travère, J.M., Le Poec, C., Courtheoux, P., Derlon, J.M., Baron, J.C., 1992. Regional cerebral oxygen consumption, blood flow, and blood volume in healthy human aging. Arch. Neurol. 49, 1013–1020.

McFadden, J.J., Matthews, J.C., Scott, L.A., Parker, G.J.M., Lohézic, M., Parkes, L.M., 2021. Optimization of quantitative susceptibility mapping for regional estimation of oxygen extraction fraction in the brain. Magn. Reson. Med. 86, 1314–1329.

Miao, X., Nayak, K.S., Wood, J.C., 2019. In vivo validation of T2- and susceptibility-based S(v) O(2) measurements with jugular vein catheterization under hypoxia and hypercapnia. Magn. Reson. Med. 82, 2188–2198.

Narciso, L., Ssali, T., Liu, L., Biernaski, H., Butler, J., Morrison, L., Hadway, J., Corsaut, J., Hicks, J.W., Langham, M.C., Wehrli, F.W., Iida, H., St Lawrence, K., 2021. A noninvasive method for quantifying cerebral metabolic rate of oxygen by hybrid PET/MRI: validation in a porcine model. J. Nucl. Med. 62, 1789–1796.

Ni, W., Christen, T., Zun, Z., Zaharchuk, G., 2015. Comparison of R2' measurement methods in the normal brain at 3 Tesla. Magn. Reson. Med. 73, 1228–1236.

Ogawa, S., Menon, R.S., Tank, D.W., Kim, S.G., Merkle, H., Ellermann, J.M., Ugurbil, K., 1993. Functional brain mapping by blood oxygenation level-dependent contrast magnetic resonance imaging. A comparison of signal characteristics with a biophysical model. Biophys. J. 64, 803–812.

Pantano, P., Baron, J.C., Lebrun-Grandié, P., Duquesnoy, N., Bousser, M.G., Comar, D., 1984. Regional cerebral blood flow and oxygen consumption in human aging. Stroke 15, 635–641.

Pauling, L., Coryell, C.D., 1936. The magnetic properties and structure of hemoglobin, oxyhemoglobin and carbonmonoxyhemoglobin. Proc. Natl. Acad. Sci. U. S. A. 22, 210–216.

Pedersen, M., Dissing, T.H., Morkenborg, J., Stodkilde-Jorgensen, H., Hansen, L.H., Pedersen, L.B., Grenier, N., Frokiaer, J., 2005. Validation of quantitative BOLD MRI measurements in kidney: application to unilateral ureteral obstruction. Kidney Int. 67, 2305–2312.

Peng, S.-L., Dumas, J.A., Park, D.C., Liu, P., Filbey, F.M., McAdams, C.J., Pinkham, A.E., Adinoff, B., Zhang, R., Lu, H., 2014. Age-related increase of resting metabolic rate in the human brain. Neuroimage 98, 176–183.

Reddy, P.H., Beal, M.F., 2005. Are mitochondria critical in the pathogenesis of Alzheimer's disease? Brain Res. Brain Res. Rev. 49, 618–632.

Rodgers, Z.B., Englund, E.K., Langham, M.C., Magland, J.F., Wehrli, F.W., 2015. Rapid T2- and susceptometry-based CMRO2 quantification with interleaved TRUST (iTRUST). Neuroimage 106, 441–450.

Rodgers, Z.B., Jain, V., Englund, E.K., Langham, M.C., Wehrli, F.W., 2013. High temporal resolution MRI quantification of global cerebral metabolic rate of oxygen consumption in response to apneic challenge. J. Cereb. Blood Flow Metab. 33, 1514–1522.

Rodgers, Z.B., Leinwand, S.E., Keenan, B.T., Kini, L.G., Schwab, R.J., Wehrli, F.W., 2016. Cerebral metabolic rate of oxygen in obstructive sleep apnea at rest and in response to breath-hold challenge. J. Cereb. Blood Flow Metab. 36, 755–767.

Ropele, S., Langkammer, C., 2017. Iron quantification with susceptibility. NMR Biomed 30, e3534.

Salomir, R., de Senneville, B.D., Moonen, C.T., 2003. A fast calculation method for magnetic field inhomogeneity due to an arbitrary distribution of bulk susceptibility. Concepts Magn. Reson. Part B Magn. Reson. Eng. Educ. J. 19, 26–34.

Schenck, J.F., 1996. The role of magnetic susceptibility in magnetic resonance imaging: MRI magnetic compatibility of the first and second kinds. Med. Phys. 23, 815–850.

Sedlacik, J., Reichenbach, J.R., 2010. Validation of quantitative estimation of tissue oxygen extraction fraction and deoxygenated blood volume fraction in phantom and in vivo experiments by using MRI. Magn. Reson. Med. 63, 910–921.

Shen, N., Zhang, S., Cho, J., Li, S., Zhang, J., Xie, Y., Wang, Y., Zhu, W., 2021. Application of cluster analysis of time evolution for magnetic resonance imaging -derived oxygen extraction fraction mapping: a promising strategy for the genetic profile prediction and grading of glioma. Front. Neurosci. 15.

Shu, C.Y., Sanganahalli, B.G., Coman, D., Herman, P., Rothman, D.L., Hyder, F., 2016. Quantitative β mapping for calibrated fMRI. Neuroimage 126, 219–228.

Spees, W.M., Yablonskiy, D.A., Oswood, M.C., Ackerman, J.J., 2001. Water proton MR properties of human blood at 1.5 Tesla: magnetic susceptibility, T(1), T(2), T*(2), and non-Lorentzian signal behavior. Magn. Reson. Med. 45, 533–542.

Stadlbauer, A., Zimmermann, M., Bennani-Baiti, B., Helbich, T.H., Baltzer, P., Clauser, P., Kapetas, P., Bago-Horvath, Z., Pinker, K., 2019. Development of a non-invasive assessment of hypoxia and neovascularization with magnetic resonance imaging in benign and malignant breast tumors: initial results. Mol. Imaging Biol. 21, 758–770.

Stone, A.J., Blockley, N.P., 2017. A streamlined acquisition for mapping baseline brain oxygenation using quantitative BOLD. Neuroimage 147, 79–88.

Stone, A.J., Blockley, N.P., 2020. Improving qBOLD based measures of oxygen extraction fraction using hyperoxia-BOLD derived measures of blood volume. bioRxiv, 2020.2006.2014.151134.

Straub, S., Stiegeler, J., El-Sanosy, E., Bendszus, M., Ladd, M.E., Schneider, T.M., 2022. A novel gradient echo data based vein segmentation algorithm and its application for the detection of regional cerebral differences in venous susceptibility. Neuroimage 250, 118931.

Sullivan, P.G., Brown, M.R., 2005. Mitochondrial aging and dysfunction in Alzheimer's disease. Prog. Neuro-Psychopharmacol. Biol. Psychiatry 29, 407–410.

Thulborn, K.R., Waterton, J.C., Matthews, P.M., Radda, G.K., 1982. Oxygenation dependence of the transverse relaxation time of water protons in whole blood at high field. Biochim. Biophys. Acta 714, 265–270.

Tohgi, H., Yonezawa, H., Takahashi, S., Sato, N., Kato, E., Kudo, M., Hatano, K., Sasaki, T., 1998. Cerebral blood flow and oxygen metabolism in senile dementia of Alzheimer's type and vascular dementia with deep white matter changes. Neuroradiology 40, 131–137.

Ulrich, X., Yablonskiy, D.A., 2016. Separation of cellular and BOLD contributions to T2* signal relaxation. Magn. Reson. Med. 75, 606–615.

Vinayagamani, S., Sheelakumari, R., Sabarish, S., Senthilvelan, S., Ros, R., Thomas, B., Kesavadas, C., 2021. Quantitative susceptibility mapping: technical considerations and clinical applications in neuroimaging. J. Magn. Reson. Imaging 53, 23–37.

Wang, X., Sukstanskii, A.L., Yablonskiy, D.A., 2013. Optimization strategies for evaluation of brain hemodynamic parameters with qBOLD technique. Magn. Reson. Med. 69, 1034–1043.

Walker, HK, Hall, WD, 1990. Hurst JW, editors. Clinical Methods: The History, Physical, and Laboratory Examinations, 3rd edn. Butterworths, Boston.

Wang, Y., Liu, T., 2015. Quantitative susceptibility mapping (QSM): decoding MRI data for a tissue magnetic biomarker. Magn. Reson. Med. 73, 82–101.

Wang, Y., Spincemaille, P., Liu, Z., Dimov, A., Deh, K., Li, J., Zhang, Y., Yao, Y., Gillen, K.M., Wilman, A.H., Gupta, A., Tsiouris, A.J., Kovanlikaya, I., Chiang, G.C., Weinsaft, J.W., Tanenbaum, L., Chen, W., Zhu, W., Chang, S., Lou, M., Kopell, B.H., Kaplitt, M.G., Devos, D., Hirai, T., Huang, X., Korogi, Y., Shtilbans, A., Jahng, G.H., Pelletier, D., Gauthier, S.A., Pitt, D., Bush, A.I., Brittenham, G.M., Prince, M.R., 2017. Clinical quantitative susceptibility mapping (QSM): biometal imaging and its emerging roles in patient care. J. Magn. Reson. Imaging 46, 951–971.

Ward, P.G.D., Fan, A.P., Raniga, P., Barnes, D.G., Dowe, D.L., Ng, A.C.L., Egan, G.F., 2017a. Improved Quantification of Cerebral Vein Oxygenation Using Partial Volume Correction. Front. Neurosci. 11.

Ward, P.G.D., Ferris, N.J., Raniga, P., Dowe, D.L., Ng, A.C.L., Barnes, D.G., Egan, G.F., 2018. Combining images and anatomical knowledge to improve automated vein segmentation in MRI. Neuroimage 165, 294–305.

Ward, P.G.D., Ferris, N.J., Raniga, P., Ng, A.C.L., Barnes, D.G., Dowe, D.L., Egan, G.F., 2017b. Vein segmentation using shape-based Markov random fields. In: 2017 IEEE 14th International Symposium on Biomedical Imaging (ISBI 2017), pp. 1133–1136.

Wehrli, F.W., Fan, A.P., Rodgers, Z.B., Englund, E.K., Langham, M.C., 2017. Susceptibility-based time-resolved whole-organ and regional tissue oximetry. NMR Biomed 30, e3495.

Weisskoff, R.M., Kiihne, S., 1992. MRI susceptometry: image-based measurement of absolute susceptibility of MR contrast agents and human blood. Magn. Reson. Med. 24, 375–383.

Wise, R.G., Harris, A.D., Stone, A.J., Murphy, K., 2013. Measurement of OEF and absolute CMRO2: MRI-based methods using interleaved and combined hypercapnia and hyperoxia. Neuroimage 83, 135–147.

Wu, D., Zhou, Y., Cho, J., Shen, N., Li, S., Qin, Y., Zhang, G., Yan, S., Xie, Y., Zhang, S., Zhu, W., Wang, Y., 2021. The spatiotemporal evolution of MRI-derived oxygen extraction fraction and perfusion in ischemic stroke. Front. Neurosci. 15.

Wu, P.H., Rodríguez-Soto, A.E., Wiemken, A., Englund, E.K., Rodgers, Z.B., Langham, M.C., Schwab, R.J., Detre, J.A., Guo, W., Wehrli, F.W., 2022. MRI evaluation of cerebral metabolic rate of oxygen (CMRO(2)) in obstructive sleep apnea. J. Cereb. Blood Flow Metab. 42, 1049–1060.

Xu, B., Liu, T., Spincemaille, P., Prince, M., Wang, Y., 2014. Flow compensated quantitative susceptibility mapping for venous oxygenation imaging. Magn. Reson. Med. 72, 438–445.

Yablonskiy, D.A., 1998. Quantitation of intrinsic magnetic susceptibility-related effects in a tissue matrix. Phantom study. Magn. Reson. Med. 39, 417–428.

Yablonskiy, D.A., Haacke, E.M., 1994. Theory of NMR signal behavior in magnetically inhomogeneous tissues: the static dephasing regime. Magn. Reson. Med. 32, 749–763.

Yablonskiy, D.A., Sukstanskii, A.L., He, X., 2013a. Blood oxygenation level-dependent (BOLD)-based techniques for the quantification of brain hemodynamic and metabolic properties–theoretical models and experimental approaches. NMR in Biomed 26, 963–986.

Yablonskiy, D.A., Sukstanskii, A.L., Luo, J., Wang, X., 2013b. Voxel spread function method for correction of magnetic field inhomogeneity effects in quantitative gradient-echo-based MRI. Magn. Reson. Med. 70, 1283–1292.

Yablonskiy, D.A., Wen, J., Kothapalli, S., Sukstanskii, A.L., 2021. In vivo evaluation of heme and non-heme iron content and neuronal density in human basal ganglia. Neuroimage 235, 118012.

Yadav, B.K., Buch, S., Krishnamurthy, U., Jella, P., Hernandez-Andrade, E., Trifan, A., Yeo, L., Hassan, S.S., Mark Haacke, E., Romero, R., Neelavalli, J., 2019. Quantitative susceptibility mapping in the human fetus to measure blood oxygenation in the superior sagittal sinus. Eur. Radiol. 29, 2017–2026.

Yamaguchi, T., Kanno, I., Uemura, K., Shishido, F., Inugami, A., Ogawa, T., Murakami, M., Suzuki, K., 1986. Reduction in regional cerebral metabolic rate of oxygen during human aging. Stroke 17, 1220–1228.

Yang, L., Cho, J., Chen, T., Gillen, K.M., Li, J., Zhang, Q., Guo, L., Wang, Y., 2022. Oxygen extraction fraction (OEF) assesses cerebral oxygen metabolism of deep gray matter in patients with pre-eclampsia. Eur. Radiol. 32, 6058–6069.

Zhang, J., Cho, J., Zhou, D., Nguyen, T.D., Spincemaille, P., Gupta, A., Wang, Y., 2018. Quantitative susceptibility mapping-based cerebral metabolic rate of oxygen mapping with minimum local variance. Magn. Reson. Med. 79, 172–179.

Zhang, J., Liu, T., Gupta, A., Spincemaille, P., Nguyen, T.D., Wang, Y., 2015. Quantitative mapping of cerebral metabolic rate of oxygen (CMRO2) using quantitative susceptibility mapping (QSM). Magn. Reson. Med. 74, 945–952.

Zhang, J., Zhou, D., Nguyen, T.D., Spincemaille, P., Gupta, A., Wang, Y., 2017b. Cerebral metabolic rate of oxygen (CMRO2) mapping with hyperventilation challenge using quantitative susceptibility mapping (QSM). Magn. Reson. Med. 77, 1762–1773.

Zhang, S., Cho, J., Nguyen, T.D., Spincemaille, P., Gupta, A., Zhu, W., Wang, Y., 2020. Initial experience of challenge-free MRI-based oxygen extraction fraction mapping of ischemic stroke at various stages: comparison with perfusion and diffusion mapping. Front. Neurosci. 14, 535441.

Zhao, Y., Wen, J., Cross, A.H., Yablonskiy, D.A., 2016. On the relationship between cellular and hemodynamic properties of the human brain cortex throughout adult lifespan. Neuroimage 133, 417–429.

Zhou, D., Cho, J., Zhang, J., Spincemaille, P., Wang, Y., 2017. Susceptibility underestimation in a high-susceptibility phantom: dependence on imaging resolution, magnitude contrast, and other parameters. Magn. Reson. Med. 78, 1080–1086.